ROYAL INSTITUTE
OF TECHNOLOGY

Calibration of the muon momentum resolution in view of the W mass measurement with the CMS experiment

GIULIA RIPELLINO

Master of Science Thesis

Supervisor CERN: Luigi Rolandi
Supervisor KTH: Jonas Strandberg
Examiner: Bengt Lund-Jensen

AUGUST 2015

TRITA-FYS 2015:57 ISSN 0280-316X ISRN KTH/FYS/–15:57–SE

Abstract

With the discovery of the Higgs boson, all components of the Standard Model have been experimentally verified. It is therefore possible to predict many observables of the model with increased accuracy. A high precision measurement of the W boson mass can be compared to the theoretical prediction, thereby allowing for an important test of the consistency and validity of the Standard Model. In CMS, the W boson mass is measured using W decays into a muon and a muon neutrino. One of the main systematic uncertainties affecting the measurement is represented by the level of understanding of the muon momentum scale and resolution.

This thesis introduces the general strategies of the W mass measurement and the calibration of the muon momentum scale and presents a new study of the muon momentum resolution. The analysis uses simulated and measured samples of J/ψ and Z dimuon events collected at $\sqrt{s} = 7\,\mathrm{TeV}$, aiming to measure the muon momentum resolution with a relative precision of 3 %. Reaching such an accuracy is essential in order to remove biases on the muon momentum scale introduced by the resolution.

Sammanfattning

I juli 2012 tillkännagav experimenten ATLAS och CMS vid CERN upptäckten av en ny partikel kompatibel med Standardmodellens Higgsboson. Med denna upptäckt är alla komponenter i Standardmodellen kända, vilket gör det möjligt att med hög precision förutspå egenskaperna hos flera elementarpartiklar. En precis mätning av W-bosonens massa kan jämföras med den teoretiska förutsägelsen och därmed användas för att testa Standardmodellens giltighet.

Vid CMS-experimentet bestäms W-bosonens massa genom att studera dess sönderfall till en myon och en myonneutrino. Precisionen begränsas till stor del av systematiska och statistiska fel i mätningen av myonens rörelsemängd. Dessa fel kan dock kontrolleras och reduceras genom noggrann kalibrering av detektorn.

Denna avhandling sammanfattar mätningen av myonens rörelsemängd och kalibreringen av de systematiska felkällorna med utgångspunkt från analysen av W-bosonens massa. Vidare presenteras en ny studie av de mätfel som uppkommer på grund av detektorns upplösning. Analysen utförs genom att studera J/ψ-mesonens och Z-bosonens sönderfall till två myoner i simuleringar och i data uppsamlad vid en kollisionsenergi på $\sqrt{s} = 7\,\text{TeV}$. Målet är att mäta detektorns upplösning med en relativ noggrannhet på 3 %. Denna precision är nödvändig för att undvika att upplösningen påverkar kalibreringen av de systematiska felkällorna.

Contents

Chapter 1

Introduction

The Standard Model (SM) of particle physics is a successful theory that describes the fundamental forces and particles in nature. Since its formulation in the 1960's and 1970's, the SM has been tested experimentally to great success and has been able to predict and explain several experimental observations. The last component of the model that was experimentally verified was the Higgs boson, whose discovery was announced in 2012 by the ATLAS and CMS collaborations at CERN [1,2]. With this discovery, it is possible to predict many observables with increased precision and thereby further test the consistency and validity of the model. Small deviations in the SM predictions from the measured values might indicate new physics at higher energy scales than have thus far been probed. A high precision measurement of the mass of the W boson, which is one of the main building blocks of the SM, allows for such a test of the agreement between theory and experiment.

At the CMS experiment, the mass of the W boson is extracted from its decay into a muon and a muon neutrino. The measurement involves fine-tuning of several observables in the decay that eventually are combined to extract the mass. One of the main systematic uncertainties affecting the measurement is represented by the level of understanding of the muon momentum scale and resolution which therefore must be calibrated to high precision. The calibration is a challenging task that requires detailed understanding of the detector effects that bias the scale and a precise modeling of the resolution in the detector. This thesis summarizes the W mass measurement and the calibration of the muon momentum scale and presents a new analysis of the muon momentum resolution. The study is performed on measured and simulated samples of J/ψ and Z decays into two muons. These events are reconstructed with high purity in CMS and therefore constitute reliable control samples.

This thesis begins with an introduction to the SM and the CMS experiment in Chapters 2 and 3, followed by a description of the W and Z bosons in Chapter 4 and the J/ψ meson in Chapter 5. The W mass measurement and the muon momentum scale calibration are then introduced in Chapters 6 and 7. Finally, the study of the muon momentum resolution is presented in Chapter 8. The thesis is concluded with a summary in Chapter 9.

1.1 The author's contribution

The analysis of the W boson mass described in this thesis is a collaborative work performed by the W mass group at the CMS experiment at CERN. The author has mainly been involved in the calibration of the muon momentum in view of the mass measurement. Chapter 7 summarizes the methodology applied by the group to calibrate the muon momentum scale and contains figures produced by the author. The study of the muon momentum resolution described in Chapter 8 is developed and carried out solely by the author.

Chapter 2

The Standard Model

The Standard Model (SM) of particle physics [3, 4] summarizes our understanding of the fundamental building blocks of nature. The SM explains how matter is built from a small number of fundamental particles and how these particles interact through the electromagnetic, the weak and the strong force.

The theoretical framework of the SM is quantum field theory (QFT), where particles are introduced as excitations of quantum fields that permeate the universe. These fields are specific to each type of particle and communicate only through the exchange of force quanta which in turn are excitations of force fields. In QFT, the SM is described by the gauge symmetry group $SU(3) \times SU(2) \times U(1)$ which defines all fundamental interactions. $SU(3)$ describes the strong force and $SU(2) \times U(1)$ describes the unified electroweak interaction.

The particle content of the SM is summarized in Table 2.1. Matter is composed of leptons and quarks which are spin-1/2 particles. They exist in three generations, with four members in each generation. The particles mediating the interactions are gauge bosons which are spin-1 particles. The photon mediates the electromagnetic force, the $W^{\pm}$ and Z bosons the weak force and the eight gluons the strong force. The last component of the SM is the spin-0 Higgs boson, whose field explains the origin of mass in the SM.

This chapter introduces the particle content of the SM and the fundamental interactions in more depth together with other useful concepts which form the theoretical background to the work presented in this thesis. For a more complete review of these subjects the reader is referred to one of the standard textbooks on the subject, e.g the book by Griffiths [5].

2.1 Matter

The fundamental constituents of matter are the spin-1/2 fermions. These obey Fermi-Dirac statistics and are subject to the Pauli exclusion principle which states that two identical fermions cannot occupy the same quantum state. Each fermion has a corresponding antiparticle, commonly denoted by an overlying bar, which has

Table 2.1: The particle content of the SM including charges in units of e, masses and lifetimes or decay widths when applicable. Values are taken from the Particle Data Group Listings [6]. Uncertainties for very precise measurements have been omitted. All quarks, except the top quark, form bound states before they decay and therefore do not have a defined mean lifetime.

	Particle	**Charge**	**Mass**	**Mean lifetime or width**
Leptons	e (electron)	-1	$0.511\,\text{MeV}$	Stable
	ν_e (e neutrino)	0	$< 2\,\text{eV}$	Stable
	μ (muon)	-1	$106\,\text{MeV}$	$2.2 \cdot 10^{-6}\,\text{s}$
	ν_μ (μ neutrino)	0	$< 2\,\text{eV}$	Stable
	τ (tau)	-1	$1776.82 \pm 0.16\,\text{MeV}$	$(290.3 \pm 0.5) \cdot 10^{-15}\,\text{s}$
	ν_τ (τ neutrino)	0	$< 2\,\text{eV}$	Stable
Quarks	u (up)	$+2/3$	$2.3^{+0.7}_{-0.5}\,\text{MeV}$	-
	d (down)	$-1/3$	$4.8^{+0.5}_{-0.3}\,\text{MeV}$	-
	c (charm)	$+2/3$	$1.275 \pm 0.025\,\text{GeV}$	-
	s (strange)	$-1/3$	$95 \pm 5\,\text{MeV}$	-
	t (top)	$+2/3$	$173.21 \pm 0.71\,\text{GeV}$	$2.0 \pm 0.5\,\text{GeV}$
	b (bottom)	$-1/3$	$4.18 \pm 0.03\,\text{GeV}$	-
Bosons	γ (photon)	0	0	Stable
	$W^\pm$	± 1	$80.385 \pm 0.015\,\text{GeV}$	$2.085 \pm 0.042\,\text{GeV}$
	Z	0	$91.1876 \pm 0.0021\,\text{GeV}$	$2.4952 \pm 0.0023\,\text{GeV}$
	g (8 gluons)	0	0	Stable
	H (Higgs)	0	$125.7 \pm 0.4\,\text{GeV}$	$\sim 4\,\text{MeV}$

the same mass and spin but opposite values of the other quantum numbers. The fermions are divided into two groups, the quarks and the leptons, where the quarks differ from the leptons in that they couple to the strong force.

2.1.1 Leptons

There are three distinct types, or flavors, of charged leptons: the electron (e^-), the muon (μ^-) and the tau (τ^-), all carrying charge $-e$. Corresponding to these are the antileptons: the positron (e^+), the antimuon (μ^+) and the antitau (τ^+), which carry charge $+e$. The flavors have identical characteristics but differ in masses and lifetimes. Each charged lepton l has an associated neutrino ν_l which is electrically neutral and has a very small mass. The lepton generations thus consist of the doublets (e, ν_e), (μ, ν_μ) and (τ, ν_τ).

Each generation is associated with a lepton number L_l which is conserved separately for each flavor in all interactions[1]. The lepton number has the value $+1$ for

[1] An exception is neutrino oscillations where conservation of flavor is violated. However, this has no practical effect in any other particle interactions.

the lepton and the neutrino in the generation, -1 for the corresponding antilepton and antineutrino and 0 for all other particles.

The charged leptons interact through the electromagnetic and weak forces whereas the neutrinos only interact through the weak force. Because of this, neutrinos can be detected only with considerable difficulty.

2.1.2 Quarks

The quarks exist in six flavors forming the three generations (u, d), (c, s) and (t, b). Each generation consists of a quark with charge $+2/3$ and a quark of charge $-1/3$, in units of e. As opposed to the leptons, the quarks are not found as free particles in nature. Instead, they are always confined to bound states called hadrons. This behavior is referred to as quark confinement. The hadrons are classified as mesons consisting of a quark and an antiquark ($q\bar{q}$) and baryons and antibaryons consisting of three quarks or three antiquarks ($qqq/\bar{q}\bar{q}\bar{q}$). Due to quark confinement, the quark masses and lifetimes cannot be measured directly. The masses of the u, d, c, s and b quarks presented in Table 2.1 are inferred indirectly from the observed masses of the bound states. The top quark has a very short lifetime and decays before it forms hadrons. Its mass can therefore be measured directly from the decay products.

The reason for quark confinement is closely associated with color, a quantum number that exists for quarks but not for leptons. Any quark can exist in three different colors: red, green and blue. Likewise, the antiquarks can exist in the three corresponding anticolors. Color neutral combinations can be formed by adding together all three colors or by adding a color to an anticolor. As it turns out, only color neutral particles exist in nature. This explains why all hadrons are formed either by a quark and an antiquark or by three quarks or antiquarks, these are the only combinations that can be made color neutral. In QFT, this concept is described in terms of the gauge symmetry group $SU(3)$ which is generated by the three colors. The various color combinations form different states, of which nature always chooses the singlet state. This state can be achieved only by combining three different colors or by combining one color and one anticolor.

Each quark has a so-called baryon number B assigned to it, $+1/3$ for the quarks and $-1/3$ for the antiquarks. Consequently, all mesons have $B = 0$, while baryons and antibaryons have $B = \pm 1$. All leptons have zero baryon number. The total baryon number is conserved in all interactions. Furthermore, each flavor is associated with a quark number where the quark counts as $+1$ and the antiquark as -1. The quark number is conserved separately for each flavor in the electromagnetic and strong interactions.

2.2 Interactions

There are four fundamental forces in our universe: the electromagnetic, the weak, the strong and the gravitational force. Of these, the first three forces are accounted for by the SM and will be described together with their force carrying bosons in

this section. The gravitational force is several orders of magnitude weaker than the other forces and is not incorporated in the SM.

All fundamental forces are mediated through the exchange of gauge bosons that carry energy and momentum between the interacting particles. The squared four-momentum transfer q^2 determines the resolution scale of the interaction. A high momentum transfer corresponds to a force mediating boson with short wavelength. This implies that interactions happening at large momentum transfer can resolve smaller distances.

The force acting between two particles is further characterized by the strength of the interaction and the range over which the interaction takes place. In each case, the strength is determined by the coupling constant of the force. This is a dimensionless quantity that specifies the strength of the force exerted in an interaction. The range R of the interaction is characterized by the mass M_X of the force mediating particle through the relation

$$R = \frac{\hbar}{M_X c}. \tag{2.1}$$

Forces mediated by massless particles are therefore in principle infinite in range whereas interactions mediated by massive particles have a finite range.

2.2.1 The electromagnetic force

The electromagnetic interaction couples to electric charge. All fundamental fermions, except the neutrinos which are electrically neutral, therefore interact electromagnetically. The interaction is mediated by the massless photon and is therefore infinite in range. All electromagnetic interactions conserve lepton numbers and individual quark numbers. The electric charge must also be conserved. Since the photon is neutral, this implies that leptons and quarks only can be created or annihilated in pairs through the electromagnetic interaction.

The electromagnetic coupling constant α is affected by pairs of virtual quarks and leptons that contribute to electromagnetic scattering processes. These virtual particles result in a vacuum polarization that partially screens the bare charge of the interacting fermions and reduces the strength of the interaction. At short distances, the screening becomes less efficient. The electromagnetic coupling strength therefore grows stronger at short distances, or equivalently, at large momentum transfer. This behavior is referred to as running of the coupling constant. At zero momentum transfer, $q^2 = 0$, the value of the coupling constant is $1/137$ and at the scale of the Z boson, $q^2 = M_Z^2$, the value is $1/128$.

2.2.2 The weak force

The weak interaction couples to weak isospin, an intrinsic property that all fermions in the SM possess. The force is mediated by the three massive gauge bosons, the Z and the $W^{\pm}$, and is therefore a short range interaction.

The interactions mediated by the $W^{\pm}$ bosons are called charged currents. These interactions do not conserve the individual quark numbers and can therefore change the quark flavor. For instance, a top quark can decay directly to a lighter quark through the process

$$t \to q + W^{+}, \tag{2.2}$$

where $q = d, s, b$. Due to quark confinement, reactions of this kind always take place within hadrons, with the $W^{\pm}$ being emitted or absorbed by the constituent quarks. The interactions mediated by the Z boson conserve flavor and are called neutral currents.

For the leptons, the charged weak current can only couple within the generations since the lepton numbers must be conserved. The possible interactions are thus:

$$l^{\pm} \to W^{\pm} + \overset{(-)}{\nu}_l \tag{2.3}$$

and

$$W^{\pm} \to l^{\pm} + \overset{(-)}{\nu}_l. \tag{2.4}$$

A lepton can decay into a lighter lepton by combining two such interactions. For instance, a muon can decay to an electron and two neutrinos according to the process

$$\begin{aligned} \mu^{-} &\to W^{-} + \nu_{\mu} \\ &\quad \big\lfloor \longrightarrow e^{-} + \bar{\nu}_e. \end{aligned} \tag{2.5}$$

2.2.3 The strong force

The strong interaction couples to color charge and therefore only to the quarks. It is mediated by the massless gluons which themselves also carry color charge. The colors can be combined in eight different ways under the $SU(3)$ symmetry, resulting in eight variations of gluons.

The strong coupling constant runs with energy. Just like the electromagnetic case, virtual pairs of fermions polarize the vacuum, leading to a reduced strength at large distances. However, in the strong interaction, also virtual pairs of gluons contribute to the running of the coupling constant. The gluon pairs lead to an antiscreening effect, meaning that they cause the interaction to grow weaker at short distances. This effect is larger than the screening correction and the net result is a running opposite to the running of the electromagnetic coupling constant. The strong interaction thus grows weaker at short distances, or equivalently, at large momentum transfer. This concept is called asymptotic freedom.

2.3 Decays and conservation laws

A general property of all fundamental particles is their tendency to decay into lighter particles if they are allowed to do so. Whether or not the decay is possible is dictated

by a number of conservation laws that permit certain reactions and forbid others. For instance, the electric charge, the color charge, the overall baryon number and the individual lepton numbers must be conserved in all interactions. There is also a set of kinematic conservation laws, such as conservation of energy and momentum, that apply to all interactions. A particle cannot spontaneously decay into a heavier particle since this would violate the conservation of energy.

The conservation laws explain why certain particles are stable. The electron is the lightest charged particle, so conservation of energy and charge prevents it from decaying. Likewise, the proton, which consists of the quarks (uud), is the lightest particle with non-zero baryon number and is therefore stable.

All unstable particles are characterized by their mean lifetimes which are summarized for the fundamental particles in Table 2.1. For a given type of interaction, the decay proceeds faster if there is a large difference in mass between the original particle and the decay products. The unstable particles are also characterized by a decay width which stems from the uncertainty principle. A measurement of the rest mass of a particle with finite lifetime will have an uncertainty that is inversely proportional to its mean lifetime. This uncertainty is referred to as the decay width Γ of the particle. A measurement of the mass of an unstable particle a large number of times results in a so-called Breit-Wigner distribution [7]. The peak of this distribution corresponds to the invariant mass and the full width at half maximum corresponds to the decay width.

2.4 Feynman diagrams and calculus

Feynman diagrams are important tools in the analysis of particle physics. They provide a convenient way to illustrate interactions of particles and are also associated with mathematical rules that allow for the calculation of quantum mechanical probabilities for the interactions to occur. In the diagrams, the fermions are represented by solid lines and the gauge bosons by dashed or curly lines. By convention, time runs from left to right with particles represented by arrows pointing to the right and antiparticles by arrows pointing to the left. According to these conventions, the decay of the muon described in Section 2.2.2, can be depicted as in Fig. 2.1.

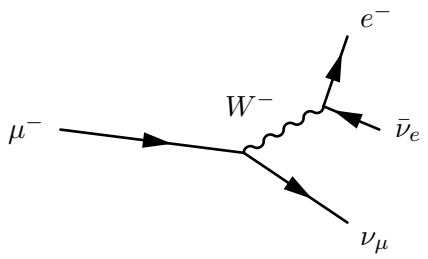

Figure 2.1: Feynman diagram for the process $\mu^- \rightarrow e^- + \bar{\nu}_e + \nu_\mu$.

Feynman diagrams and Feynman rules are important for the calculation of cross sections in particle physics. The cross section describes the probability of a given process to occur and is determined by two components: the phase space factor and the matrix element. The phase space factor describes the number of kinematically available states for the final state particles to occupy. It depends on the masses, energies and momenta of the involved particles. For instance, the decay of a heavy particle involves a large phase space factor since there are many different lighter particles and therefore also many different final states. The matrix element describes the dynamics of the interaction and enters the cross section in quadrature. This part can be computed using Feynman rules which translate the diagrams into the mathematical components entering the calculation.

In quantum mechanics, a process can be modeled using the formalism of perturbation theory. The matrix element is then computed by adding up the terms in the perturbation series. Each term is depicted as a Feynman diagram and the corresponding contribution to the matrix element is calculated using Feynman rules. According to these rules, each vertex in a diagram represents a factor g which describes the strength of the interaction. For the electromagnetic interaction this constant is simply given by $g_e = e$. Since the matrix element enters the cross section in quadrature, the coupling constant is defined as a parameter proportional to the square of the coupling strength. For the electromagnetic force this is $\alpha = e^2/4\pi\epsilon_0 = 1/137$. For the weak and strong interactions, the coupling constants are denoted by α_W, α_Z and α_s.

Since a perturbation series has an infinite number of terms, there are an infinite number of Feynman diagrams describing the same process. In general the terms in the series become smaller and smaller and eventually negligible. This means that it is often justified to include only a limited number of Feynman diagrams in the calculation of the matrix element. The lowest order terms in the series are represented by Feynman diagrams at tree level, involving no loops. For the simplest processes, these contain only two vertices. Figure 2.2 shows first and second order diagrams for the scattering process $e^- + e^- \to e^- + e^-$.

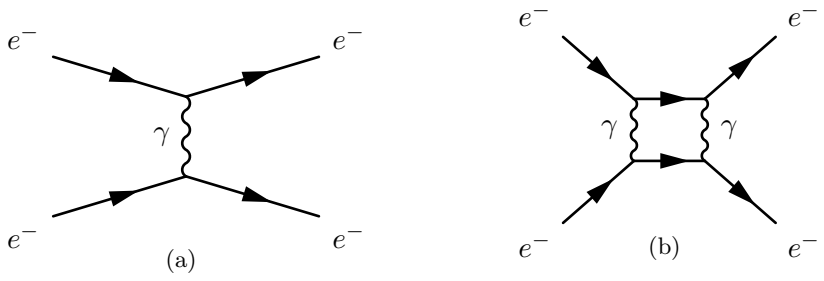

Figure 2.2: First and second order Feynman diagrams contributing to the scattering process $e^- + e^- \to e^- + e^-$.

At tree level this process contains two vertices whereas the second order diagram contains four vertices. Each vertex represents a factor of $\alpha = 1/137$ in the cross section which implies that the second order contribution to the cross section will be suppressed by a factor of $\alpha^2 = 1/137^2$ compared to the tree level contribution.

2.5 Electroweak physics

The electroweak interaction is the unified description of the electromagnetic and the weak force. Although these two forces appear very different at low energies, the theory models them as two different aspects of the same interaction. Mathematically, the unification is accomplished under the $SU(2) \times U(1)$ gauge group and allows for a gauge invariant theory for the weak interaction.

Gauge invariance is a fundamental symmetry associated with theories in which the force carriers are spin-1 bosons. For the electromagnetic interaction, this corresponds to the conservation of electric charge and for the strong interaction it corresponds to the conservation of color charge. As it turns out, a gauge invariant theory for the weak force is only possible in a mathematical framework that, in addition to the $W^{\pm}$ bosons, introduces the photon and the Z boson as mixtures of two additional electroweak bosons. This unifies the electromagnetic and the weak forces into one electroweak interaction that is gauge invariant.

2.5.1 The unification condition and the W boson mass

In the unified theory, the electromagnetic and weak coupling strengths e, g_Z and g_W are related according to the so-called unification condition

$$\frac{e}{2\left(2\epsilon_0\right)^{1/2}} = g_W \sin\theta_W = g_Z \cos\theta_W, \tag{2.6}$$

where the weak mixing angle θ_W is defined through the relation

$$\cos\theta_W = \frac{M_W}{M_Z}. \tag{2.7}$$

The unification condition can be used to predict the W boson mass in the SM. At tree level, the charged current coupling strength is characterized by the Fermi constant G_{F} according to

$$\frac{G_{\mathrm{F}}}{\sqrt{2}} = \frac{g_W^2}{M_W^2}. \tag{2.8}$$

Together with Eq. 2.6 this provides an expression for the W boson mass,

$$\left(M_W^0\right)^2 = \frac{\pi\alpha}{\sqrt{2}G_{\mathrm{F}}\sin^2\theta_W} = \frac{\pi\alpha}{\sqrt{2}G_{\mathrm{F}}\left(1 - \dfrac{M_W^2}{M_Z^2}\right)}, \tag{2.9}$$

where α is the electromagnetic coupling constant.

For a correct prediction of the mass, also higher order processes must be taken into account. The most important higher order diagram involves loops of fermions as shown in Fig. 2.3.

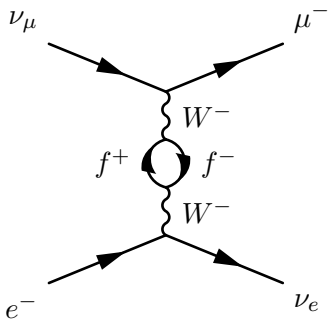

Figure 2.3: Higher order diagram that contributes to the reaction $e^- + \nu_\mu \rightarrow \mu^- + \nu_e$.

The effective mass that enters the Feynman calculation for the W boson mass is therefore affected by corrections introduced by the masses of the fermions. The top quark is by far the most massive fermion and will provide the dominant contribution. Equation 2.9 is therefore modified to

$$M_W^2 = (\rho + 1) \left(M_W^0 \right)^2 , \tag{2.10}$$

where the parameter ρ depends on the square of the top quark mass [6]. Another important higher order correction arises from loops containing the Higgs boson. These decrease the W mass with a contribution proportional to the logarithm of the Higgs mass [6].

2.5.2 The electroweak fit

Any parameter in the SM can be predicted by performing a fit of the model to all experimental observables except for the one of interest. Fits of this kind have substantially contributed to the knowledge of the SM. The electroweak fit focuses on the parameters describing the electroweak sector. After the discovery of the Higgs boson in 2012, all parameters of the SM are known and it is therefore possible to overconstrain the SM at the electroweak scale and predict important parameters to assert its validity.

The key parameters of the fit are the mass of the Z boson, the electromagnetic coupling constant and the Fermi constant, which define the electroweak sector at tree level according to Eq. 2.9. These parameters have all been determined experimentally with high precision. The Z boson mass was measured at the electron-positron collider LEP [8], the electromagnetic coupling constant is determined from the electron magnetic moment [9] and the Fermi constant is measured from the muon lifetime [9]. The fit must also include the top quark mass, the strong coupling

constant and the mass of the Higgs boson which enter at second order. Table 2.2 shows an excerpt from the result of the global electroweak fit after the discovery of the Higgs boson. The fit converges at a global minimum value of $\chi^2 = 17.8$, obtained for 14 degrees of freedom, showing that the SM accurately describes all electroweak measurements.

The electroweak global fit after the Higgs discovery leads to a value of the W mass of $80.358 \pm 0.008\,\text{GeV}$ [10] where the dominant uncertainty is given by the top quark mass [10]. This number can be compared to the world average experimental value which is $80.385 \pm 0.015\,\text{GeV}$ [6]. As opposed to other key parameters in the SM, such as the Z boson mass, the experimental uncertainty on the W mass is higher than the uncertainty on the prediction from the electroweak fit. This is a motivation for the achievement of a measurement with improved precision.

Table 2.2: Excerpt from the result of the global electroweak fit after the discovery of the Higgs boson [10]. The second column contains the world average experimental values used as input to the fit and the third column contains the values obtained from the fit to all experimental observables except for the one in the line.

Parameter	**Experimental value**	**Fit result**
M_H [GeV]	125.14 ± 0.24	93^{+25}_{-21}
M_W [GeV]	80.385 ± 0.015	80.358 ± 0.008
Γ_W [GeV]	2.085 ± 0.042	2.091 ± 0.001
M_Z [GeV]	91.1875 ± 0.0021	91.200 ± 0.011
Γ_Z [GeV]	2.4952 ± 0.0023	2.4946 ± 0.0016
m_t [GeV]	173.34 ± 0.76	$177.0^{+2.3}_{-2.4}$

Chapter 3

The CMS experiment at the LHC

3.1 The Large Hadron Collider

The Large Hadron Collider (LHC) [11] is a circular proton-proton collider operating at the European Organization for Nuclear Research (CERN). It is an accelerator with a circumference of 27 km, which makes it the world's largest collider.

The LHC is contained in an underground tunnel situated on the border between Switzerland and France. The tunnel contains two adjacent parallel beam pipes kept at ultra-high vacuum. At operation, the pipes contain proton beams[1] that circulate in opposite directions around the ring. The beams are guided around the accelerator ring by a strong magnetic field of 8.33 T maintained by 1232 superconducting dipole magnets. In addition, a total of 392 quadrupole magnets are used to focus the beam.

The LHC is a synchrotron accelerator. Acceleration is achieved as the beam repeatedly traverses a number of radio frequency cavities where energy is given to the particles. In practice, the protons are accelerated in bunches, each bunch being synchronized with the radio frequency field. The magnetic field that guides the beams grows synchronously with the energy of the protons. Once the maximum field is achieved, the coasting beams are brought into collision at four points around the ring. At these points the beam pipes are intersected, causing the beams to collide almost head on.

Before injection into the LHC, the protons are accelerated in various steps that successively increase their energy. The chain starts with a linear accelerator followed by three synchrotron accelerators of increasing size. The protons are eventually injected into the main accelerator with an energy of 450 GeV. A typical operation corresponds to about three hours to prepare the beams and about ten hours of collisions.

The four intersection points at the LHC host the experiments ALICE, ATLAS, CMS and LHCb that are dedicated to the study of the physical processes that occur in the proton-proton collisions. ATLAS and CMS are general-purpose detectors designed to cover the widest possible range of physics at the LHC. ALICE specializes

[1] The LHC also runs with beams of lead ions.

in the study of quark-gluon plasma and LHCb in the study of asymmetries between matter and antimatter.

The work presented in this thesis is an analysis carried out on data recorded by the CMS experiment. After an introduction to some important concepts at hadron colliders, this chapter is therefore devoted to a more in-depth description of the CMS experiment.

3.1.1 Luminosity and beam energy

The physics potential of a collider can be quantified in terms of the beam energy and the luminosity. The beam energy dictates the achievable center of mass energy $\sqrt{s}$, which is the energy available to create new particles. For a collider where two equal beams of energy E_{beam} are made to collide at very small crossing angle, the center of mass energy is given by

$$\sqrt{s} = 2 \cdot E_{\text{beam}}. \tag{3.1}$$

The maximum beam energy is directly proportional to the bending dipole magnetic field and to the ring circumference. For a hadron collider, the total center of mass energy is not available for particle production since the hadrons are composite particles. This is further discussed in Section 3.1.3.

The luminosity is essentially a measure of the amount of data that the collider produces. This quantity depends on the number of particles in each bunch, the frequency of complete turns around the ring, the number of bunches and the beam cross sectional area. The instantaneous luminosity $\mathcal{L}$ dictates the rate of a given process according to the equation

$$\mathcal{L} = \frac{1}{\sigma}\frac{\mathrm{d}N}{\mathrm{d}t}, \tag{3.2}$$

where σ is the cross section and $\mathrm{d}N/\mathrm{d}t$ is the rate of events of the process. The instantaneous luminosity is commonly measured in units of $\mathrm{cm}^{-2}\mathrm{s}^{-1}$.

The total number of events is obtained by integrating Eq. 3.2,

$$N = \sigma \int \mathcal{L}\mathrm{d}t. \tag{3.3}$$

In this equation, the quantity $\int \mathcal{L}\mathrm{d}t$ is referred to as the integrated luminosity and is commonly measured in units of inverse barn[2], b^{-1}. The integrated luminosity is often quoted as a description of the performance of the machine and the amount of data available for analysis. The most interesting processes for analysis typically have a very small cross section compared to the total proton-proton cross section and will be very rare at the LHC. A high luminosity is therefore needed in order to collect sufficient statistics.

The LHC is designed to operate at a center of mass energy of 14 TeV and an instantaneous luminosity of $1 \cdot 10^{34}\,\mathrm{cm}^{-2}\mathrm{s}^{-1}$ [11].

[2] $1\,\mathrm{b} = 10^{-28}\,\mathrm{m}^2$.

3.1.2 Anatomy of an event

When two proton bunches cross at any of the four intersection points at the LHC, a number of interactions take place. A proton consists of quarks and gluons which collectively are called partons. In a high q^2 proton-proton collision, the fundamental interaction takes place between individual partons and not between the protons as whole. Such processes are called hard interactions and result in the production of high momentum particles. Some of these are heavy and decay quickly into lighter particles. The end products travel into the detector with some energy and direction that are measured by the detector and stored for analysis. A particle interaction that has been captured and recorded by the detector is called an event.

In addition to the end products from the hard interaction, other processes contribute to the signature in the detector. These processes are of two kinds: underlying events and pile up. The underlying events are particles originating from the constituents of the protons that do not participate in the hard interaction. Pile up refers to interactions between other protons in the bunch and results in additional interaction vertices. At the LHC design luminosity, up to 50 interactions are expected in each bunch crossing. This must be taken into account in the event reconstruction and the primary vertex must be separated from the pile up vertices.

3.1.3 Parton distribution functions

The energy available in a hard interaction is determined by the fractions of the proton energy carried by the interacting partons. The momentum distributions of the partons within the proton are called parton distribution functions (PDFs). They represent the probability densities to find a parton carrying a momentum fraction x at an energy scale q^2. At a proton-proton center of mass energy $\sqrt{s}$, the energy available for the partonic interaction is given by $\sqrt{s}x_1x_2$, where x_1 and x_2 are the momentum fractions of the two interacting partons.

The PDFs are probabilistic functions and cannot be calculated from first principles. Experimentally determined distributions are instead available from several groups worldwide. The PDFs at a given value of x can be scaled using the DGLAP equations which describe their q^2 dependence [12]. This way, PDFs measured at other experiments can be used to build models for the collisions at the LHC.

3.1.4 Coordinates and kinematic variables

The coordinate system used by the experiments at the LHC is a right handed system with the origin at the nominal collision point. The x axis points towards the center of the LHC ring, the y axis points upwards and the z axis points along the counter clockwise beam direction. In addition, the radius r is measured from the origin in the xy plane, the azimuthal angle ϕ is measured from the x axis in the xy plane and the polar angle θ is measured from the positive z axis.

Since the quarks typically carry different fractions of the proton momentum, the center of mass frame of a collision does not necessarily coincide with the laboratory

frame. However, the momentum distribution of the partons in the plane transverse to the beam direction is negligible, which implies that the center of mass frame only moves along the beam axis. This calls for a description of particles using a special set of kinematic variables.

The relativistic phase space of a particle is usually described by the four-momentum coordinates (E, p_x, p_y, p_z). Of these, only p_x and p_y are invariant with respect to boosts along the z direction. A more suitable choice of variables which explicitly reflects the invariance of the phase space element is given by the coordinates (p_T, y, ϕ, m). Here, ϕ is the usual azimuthal angle, m the invariant particle mass, p_T the transverse momentum given by

$$p_T = p \sin\theta, \tag{3.4}$$

and y the rapidity defined as

$$y = \frac{1}{2}\ln\left(\frac{E + p_z}{E - p_z}\right). \tag{3.5}$$

The transverse momentum, the azimuthal angle and the mass are invariant under boosts along the z axis and the rapidity changes only by an additive constant. The difference in rapidity between two particles is therefore invariant under boosts along the z axis.

A measurement of the rapidity requires knowledge of both the energy and the momentum of the particle. Another useful quantity that is easier to measure is the pseudorapidity η defined as

$$\eta = -\ln\left(\tan\frac{\theta}{2}\right). \tag{3.6}$$

The pseudorapidity can simply be measured from the polar angle and is approximately equal to the rapidity for $p \gg m$, $\theta \gg 1/\gamma$ and $\pi - \theta \gg 1/\gamma$, where γ is the Lorentz factor. For light particles such as electrons and muons, the pseudorapidity is therefore preferred over rapidity. Furthermore, the pseudorapidity is often paired with the azimuthal angle ϕ to describe the angle of emission of a particle from an interaction vertex. In this system, $\eta = 0$ corresponds to the transverse plane, positive values to the forward direction and negative values to the backward direction along the z axis.

Another important quantity at hadron colliders is the missing transverse energy

$$\mathbf{E}_T^{\text{miss}} = -\sum \mathbf{p}_T, \tag{3.7}$$

where the sum is the vectorial sum taken over all reconstructed particles in an event. Since the colliding partons have negligible transverse momentum, the sum of all end product momenta in the transverse plane must be zero. The missing transverse energy is therefore an important tool to infer the presence of particles that do not give a signature in the detector.

3.1.5 Operational history of the LHC

The LHC began its planned research program in the spring of 2010 with a center of mass energy of 7 TeV. By the end of 2011, the CMS experiment had collected a total integrated luminosity of $5.6\,\mathrm{fb}^{-1}$ with a record peak luminosity of $4.0 \cdot 10^{33}\,\mathrm{cm}^{-2}\mathrm{s}^{-1}$ [13]. In 2012, the center of mass energy was increased to 8 TeV and higher instantaneous luminosities were achieved. The total integrated luminosity collected by CMS during this year amounted to $22\,\mathrm{fb}^{-1}$ with a record peak luminosity of $7.7 \cdot 10^{33}\,\mathrm{cm}^{-2}\mathrm{s}^{-1}$ [13]. The increased luminosity entails a higher sensitivity to rare processes but also poses a significant challenge to the event reconstruction. The 2012 data is characterized by approximately twice the number of interactions per bunch crossing, resulting in more complex events. In both runs, the LHC was operated with a bunch spacing of 50 ns corresponding to a collision frequency of 20 MHz. The analysis presented in this thesis is carried out on the dataset from 2011.

In the beginning of 2013, the LHC was shut down to prepare the collider to run at higher energy and luminosity. The accelerator was reactivated in early 2015, operating at a center of mass energy of 13 TeV.

3.2 The CMS experiment

The Compact Muon Solenoid (CMS) is one of two general-purpose detectors at the LHC. It has a broad physics program ranging from the study of the SM to the search for physics beyond the SM, such as supersymmetry and dark matter [14]. This section gives a brief overview of the CMS experiment and the various detector components. Emphasis is put on the tracker, the magnetic field and the muon system since understanding of these components is important for the work presented in this thesis. A complete description of the CMS experiment can be found in Reference [15].

3.2.1 Detector overview

The CMS detector is roughly cylindrical, 21.5 m long and with an outer radius of 7 m. Figure 3.1 shows the structure of the detector. The experiment consists of the cylindrical barrel at $|\eta| \leq 1.2$ and the endcaps at $|\eta| > 1.2$. Together, these two parts cover most of the solid angle around the interaction point. The detector is composed of several subdetectors that form layers at increasing values of the radius in the barrel and increasing values of z in the endcaps. Each layer serves a separate purpose in the detection and identification of particles in the detector.

The experiment is built around a huge solenoid magnet. This takes the form of a cylindrical coil of superconducting cable that generates a magnetic field of 3.8 T. The magnetic field is confined by a steel yoke that forms the bulk of the detector and supports the structure. The inside of the magnetic coils hosts the tracker, the electromagnetic calorimeter (ECAL) and the hadronic calorimeter (HCAL). On the

outside of the solenoid, the magnetic field is contained and returned by a 12-sided iron structure. This structure also hosts the large muon detectors which form the last layer of the CMS experiment.

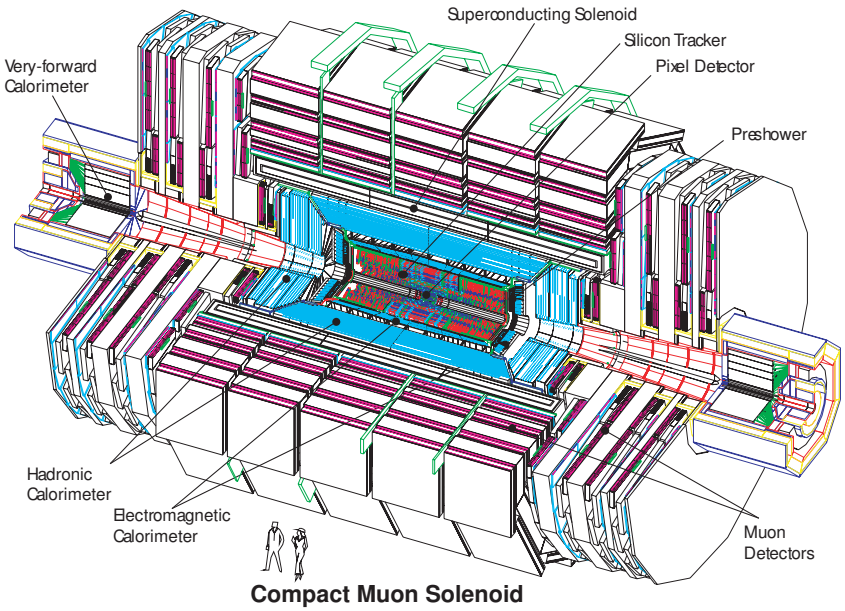

Figure 3.1: Overview of the CMS experiment [15].

Tracker The tracker[3] is the innermost subdetector and therefore closest to the interaction point. This part of the experiment is used to observe charged particles and to measure their momentum from the curvature of the tracks in the magnetic field. The tracker is made entirely of silicon, with pixel detectors in the inner region, closest to the beam, and microstrip detectors in the outer region. When a charged particle passes though the silicon it knocks electrons off the valence band, thus creating electron-hole pairs. In the presence of an externally applied electric field the electrons and the holes are separated and collected at the electrodes, producing a signal proportional to the energy lost by the passing particle. The tracker measures 5.4 m in length and 1.1 m in radius and the coverage extends up to $|\eta| = 2.5$.

Calorimeters The ECAL is designed to absorb electrons and photons, thereby allowing for a measurement of the energy of these particles. When a photon or an electron enters the calorimeter it interacts with the material, creating a shower of secondary electrons and photons. The ECAL is an homogeneous calorimeter made

[3]The tracker is discussed in more detail in Section 3.2.5.

of lead tungstate which is a very dense material, ideal for containing the electromagnetic shower. It is also a highly transparent material that scintillates when the secondary electrons move through it. The total light produced is proportional to the energy of the initial particle and is read out by photodiodes producing a signal used to reconstruct the energy deposited in the detector. The ECAL consists of a barrel section and two endcaps covering up to $|\eta| = 3$. The thickness of the ECAL is 23 cm in the barrel and 22 cm in the endcaps.

The HCAL is designed to detect and absorb hadrons in order to measure their energy. It consists of layers of brass interleaved with tiles of plastic scintillators, read out by photodiodes. The brass layers stop the particles and the scintillating layers give the signal necessary to reconstruct the particle energy. This combination was designed to allow the maximum amount of absorbing material inside of the solenoid. The HCAL consists of a barrel section and two endcaps covering up to $|\eta| = 3$. The thickness in the barrel amounts to 1.2 m.

Both the ECAL and the HCAL are contained within the solenoid. This solves a problem seen in other detector designs where energy losses in the magnet lead to uncertainties in the energy measurement. The calorimeters are complemented in the high pseudorapidity region by two forward hadronic calorimeters (HF) which extend the coverage up to $|\eta| = 5$. These subdetectors consist of layers of steel for absorption and quartz fibers read out by photomultiplier tubes. The HF is equipped to distinguish between leptons and hadrons.

Muon chambers The muon system[4] uses different types of gaseous detectors to detect and identify muons. When a muon passes through the gas it ionizes the atoms, thus creating electron-ion pairs. The electrons drift under the influence of an applied electric field and are collected at thin anode wires producing the read-out signal.

3.2.2 Particle identification

The various parts of the CMS detector work together to identify particles and to reconstruct the events recorded by the experiment. The only particles that are long lived enough to travel through the detector are photons, electrons, muons, neutrinos and some hadrons. Each kind of particle gives a different signature in the detector, as shown in Fig. 3.2.

The signals from the tracker and the ECAL are used to differentiate electrons and photons. An electron leaves a signature both in the tracker and in the ECAL whereas a photon is detected only in the ECAL. Hadrons leave a signature in the tracker if they are charged and also deposit some energy in the ECAL but typically leave the largest signature in the HCAL. This allows for hadrons to be distinguished from electrons and photons. Muons leave traces in the inner subdetectors, but they are the only charged particles that penetrate all inner layers without being com-

[4]The muon detector is discussed in more detail in Section 3.2.8.

pletely absorbed. A signature in the muon system therefore indicates the presence of a muon. Neutrinos cannot be detected, since they only interact weakly, but their presence among the final state particles can be inferred from the missing transverse energy.

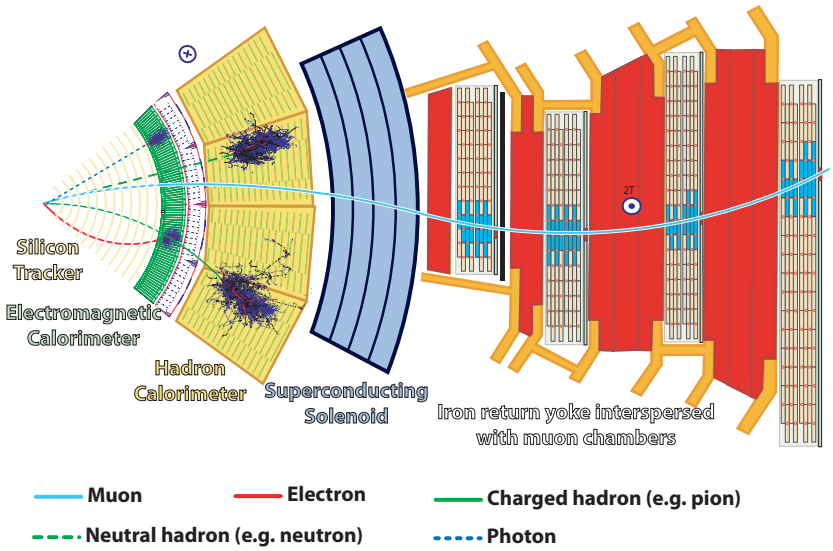

Figure 3.2: A slice of the CMS detector with the signatures of different particles [16].

3.2.3 Triggering

With a collision frequency of 20 MHz and up to 50 interactions per bunch crossing, huge amounts of data are produced every second at the LHC. It is impossible to fully process and store all the information at the rate dictated by the collision frequency. A drastic cut must therefore be made in real time at the experiment. For every event, a very fast decision must be taken, determining whether or not it should be kept for analysis. One of the most important aspects of any experiment at the LHC is therefore the trigger, which makes the online event selection. The task of the trigger is to identify possible interesting processes which implies that the selection must be based on the physics content of the events.

In CMS, the triggering system is composed of two steps, the Level-1 Trigger (L1) and the High-Level Trigger (HLT). The L1 holds all the data from each crossing in buffers while using a small amount of key information from the calorimeters and the muon system to identify features of interest. This first step is completed in about 1 µs, and reduces the rate down to 100 kHz. The L1 calculations are done on custom built hardware directly at the detector.

If an event is selected by the L1 it is passed on to the HLT. The reduced event rate allows for a more detailed analysis and more complex calculations. The HLT

therefore employs simplified versions of the software used for off-line event reconstruction and runs on ordinary computer servers. The HLT reduces the event rate further down to a few 100 Hz. The events that pass both trigger levels are stored for future analysis.

3.2.4 Magnetic field and momentum measurement

The solenoid magnet is the central device around which the CMS experiment is built. It produces a magnetic field of 3.8 T which to first approximation is homogeneous and parallel to the z axis in the tracker region. This allows for a momentum measurement of charged particles from the curved track that they follow in the magnetic field.

The path of a charged particle in a magnetic field is described by a helix with its axis parallel to the direction of the field. The bending radius of the trajectory depends on the momentum of the particle and the strength of the magnetic field. For a uniform field B, the transverse momentum of the particle is given by

$$p_T = qBr, \tag{3.8}$$

where q is the charge and r is the bending radius. Technically, the quantity measured in the tracker is the sagitta of the trajectory which is given by

$$s = \frac{L^2}{8r} = \frac{qBL^2}{8p_T}, \tag{3.9}$$

where L is the length of the track measured on the transverse plane, defined by the outer radius of the tracker.

3.2.5 Tracker

Several crucial aspects of particle identification and event reconstruction depend entirely on information from the tracker. It is therefore essential to reconstruct particle trajectories in the tracker with very high momentum, angle and position resolution. At the same time, the tracker must be light-weight in order to disturb passing particles as little as possible. The CMS tracker is specifically designed to take position measurements so accurate that tracks can be reliably reconstructed using only a few measurement points.

The tracker is composed of 1440 silicon pixel modules and 15148 silicon microstrip modules organized in layers around the interaction point. As particles travel through the tracker the pixels and microstrips in the layers produce electric signals that are detected. These hits are then stringed together to reconstruct the trajectory of the particle. The tracker consists of 13 layers in the barrel and 14 layers in the endcaps, which correspond to the typical amount of hits used to reconstruct a track. The tracker layers are shown schematically in Fig. 3.3.

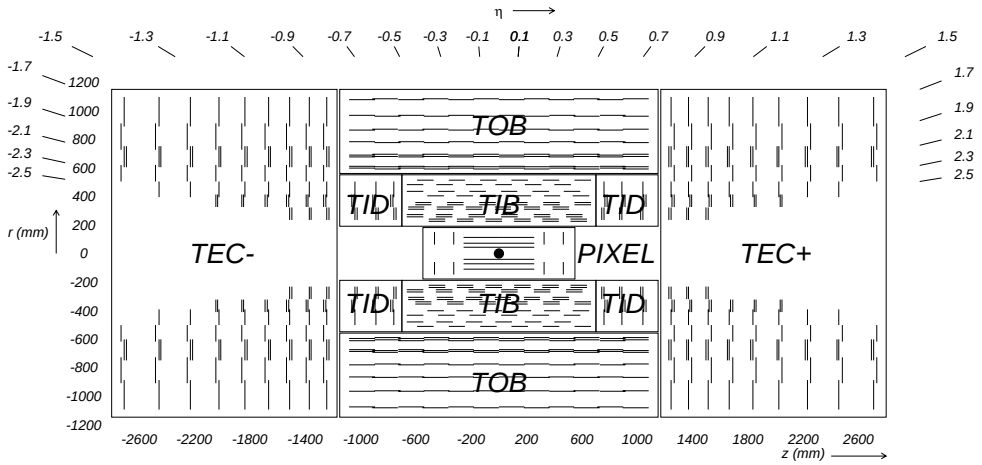

Figure 3.3: Schematic cross section through the CMS tracker [17]. Each line-element represents a detector module. Closely spaced double line-elements indicate back-to-back silicon strip modules, in which one module is tilted in order to permit reconstruction of the hit positions in three dimensions.

Pixels

The flux of particles is very high close to the interaction point. In order to reconstruct the individual tracks, a high granularity is therefore needed. This is ensured by the pixel modules that form the inner layers of the tracker.

The pixel modules in the barrel are arranged in three concentric layers situated at radii of 4.4 cm, 7.3 cm and 10.2 cm. These are complemented in the endcaps by two disks extending from 6 cm to 15 cm in radius at 34.5 cm and 46.5 cm from the nominal interaction point. The design ensures the existence of three measurement points for each track almost over the full covered range.

The modules are composed of pixels with a size of 100 µm × 150 µm with the larger side along the z coordinate. The modules provide a two-dimensional measurement of the hit position in terms of the r-ϕ and the z coordinates. The ionization signal is typically shared between two adjacent pixels which allows for a position measurement with a resolution better than the pixel size. This way, a resolution of about 15 µm is achieved.

Strips

Further away from the interaction point, the density of tracks is lower and silicon microstrip modules are used instead of pixel modules. The inner silicon strip tracker consists of the tracker inner barrel (TIB) composed of four layers and the tracker inner disks (TID) which form three endcap layers. The outer part consists of the

tracker outer barrel (TOB) composed of six layers and the tracker endcaps (TEC) composed of nine disks. Within a given layer, each module is shifted slightly in r in the barrel and in z in the endcap in order to overlap with its neighbor, thereby avoiding gaps in the acceptance. The small overlaps are also important for the alignment of the tracker which is discussed in Section 3.2.7.

The typical silicon strip module size is $10\,\text{cm} \times 5\,\text{cm}$ with a strip pitch of $80\,\mu\text{m}$ in the inner regions and $20\,\text{cm} \times 10\,\text{cm}$ with a strip pitch of $140\,\mu\text{m}$ in the outer regions. In the barrel, the strips are parallel to the z axis and in the endcap they are placed along the radial coordinate. The modules provide a measurement of the r-ϕ coordinate with a resolution of $20 - 50\,\mu\text{m}$.

In order to measure the z coordinate in the barrel and the r coordinate in the endcap with a precision better than the strip length, some of the layers carry an additional set of modules. These are tilted with respect to the regular modules by an angle of $100\,\mu\text{rad}$. Matching the hits on the tilted layers with the ones on the regular modules allows for a measurement of the third coordinate.

3.2.6 Track reconstruction

Track reconstruction refers to the process of using the hits in the tracker to obtain estimates for the momentum and position of the charged particles responsible for the hits. In total, five parameters are needed to describe the helical path: two coordinates for the origin of the trajectory, the angles η and ϕ of emission and the radius of curvature in the magnetic field.

The basic idea of the track reconstruction is to propagate the helix parameters layer by layer and fitting them to the hits. When a particle travels through the tracker it ionizes the atoms in the material and thereby loses energy. This effect must be taken into account in the track reconstruction as well as any inhomogeneities in the magnetic field. The information needed at each layer therefore includes the location and uncertainty of the detected hits, the amount of material crossed and a map of the magnetic field in the tracker.

The computation of the track parameters is performed using a Kalman filter technique [18,19]. This is an efficient mathematical method to estimate the state of a dynamic system from a series of measurements with corresponding uncertainties. In the track reconstruction, the state is characterized by the helix parameters and is iteratively estimated from the set of hits. For every tracker layer, the state is updated with the best estimation compatible with the detected hits. The parameters are updated using a weighted average, with more weight being given to estimates with high certainty. The final output is the full set of helix parameters and the full covariance matrix describing the correlations of the parameters and their errors.

3.2.7 Tracker alignment

In order to properly reconstruct particle trajectories, the positions of the tracker components must be known to a precision better than the intrinsic resolution of the

modules. Any flaw in the modeling of the tracker geometry leads to a bias in the reconstructed track which then propagates to the momentum measurement. The tracker must therefore be carefully aligned.

The basic idea of the alignment procedure is to use reconstructed tracks and make them fit better to the hits by adjusting the assumed positions of the modules. All possible deviations from the true positions are described by a set of alignment parameters that are varied systematically in the track reconstruction. The values that provide the best fit in terms of the sum of the χ^2 of all tracks are then taken as the correct alignment parameters. The first step in the procedure is to adjust the absolute position and orientation of the tracker relative to the magnetic field. This is done using two alignment parameters that describe the tilts around the x and y axes. After the adjustment of the tracker as a whole, all individual modules are aligned. The position of each module is parametrized using nine parameters. Three of these describe the translational shift of the module from the nominal position and three describe the rotational shift. The last three parameters describe any deviations in the module geometry from a flat plane. The fit of the alignment parameters is simplified by the overlaps of adjacent modules. Tracks that pass through the overlap constrain the relative position of two adjacent modules, which results in a tight constraint on the circumference of each barrel layer and each endcap ring.

A major difficulty in the alignment procedure is caused by so-called weak modes. These result from combinations of alignment parameters that do not change the track-hit residuals and therefore do not alter the total χ^2. A weak mode can result for instance from a twist where modules are moved coherently in ϕ by an amount proportional to the position along the z axis.

The alignment is performed using cosmic ray data as well as data recorded during the LHC operations. The tracker geometry is found to be very stable with time and the statistical accuracy of the alignment procedure is such that misalignment effects are small compared to the intrinsic hit resolution of the modules [20]. The alignment therefore provides a tight constrain on the local scale of the tracker and further calibrations are needed only to correct for distortions induced by the weak modes.

3.2.8 Muon detector

Muons are an important tool in the CMS physics program. They are the only charged particles that pass all inner detector layers without being absorbed and can therefore be reconstructed with very high purity even at the very first triggering levels.

The muon system is shown schematically in Fig. 3.4. It is composed of different types of gas detectors organized in layers in the return yoke of the magnet. In the barrel, up to $|\eta| = 1.3$, the muon system consists of four layers occupied by drift tube chambers (DTs). These measure the position of the muon by converting the electron drift time to the anode wire to a distance. In the endcaps, between $0.9 < |\eta| < 2.4$ where the flux of muons is higher, a different technology is used.

Four layers occupied by cathode strip chambers (CSCs) are used in each endcap. In these chambers, closely spaced anode wires are stretched between two cathodes. The ionization electrons drift towards the closest anode wire which provides the measurement point. The magnetic field is almost completely confined within the steel return yoke and the trajectories are not bent within the layers of the muon system. Each layer measures the straight track and provides a vector in space called track segment. The segments are then extrapolated between the stations to reconstruct the full track. In order to get a fast signal for triggering, resistive plate chambers (RPCs) are installed in most of the detector, up to $|\eta| = 2.1$. These are parallel plate gaseous detectors that combine an adequate position resolution with a very fast response time.

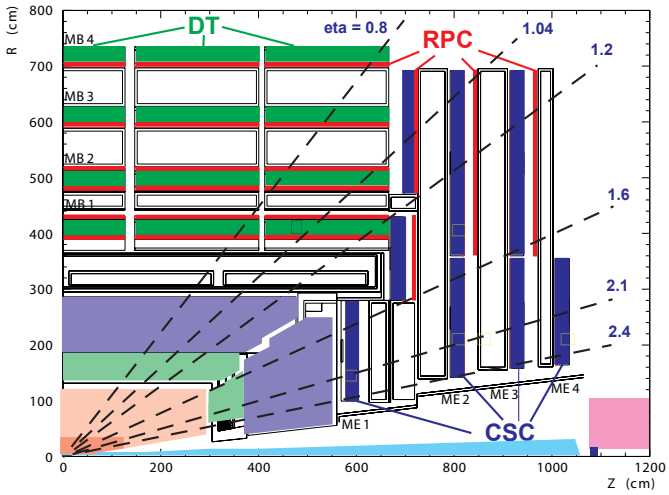

Figure 3.4: Layout of one quadrant of CMS [15]. The four DT stations in the barrel are shown in green, the four CSC stations in the endcap in blue, and the RPC stations in red.

3.2.9 Muon identification and reconstruction

A muon is identified by a signal in the muon detectors and reconstructed by combining information from the muon system with information from the tracker. Even though muons are not stopped in the inner detector layers they loose some energy in the material. On average, a muon in the barrel loses 3 GeV of transverse momentum before it reaches the first muon station and another 3 GeV between the first and the last muon station. Muons with lower energy can therefore not be reconstructed.

In the standard CMS procedure, tracks are first reconstructed independently in the tracker and the muon system. The tracks are then combined either by matching the muon system tracks with the tracker tracks, or starting from the tracker looking for matching track segments in the muon system. The latter is efficient for low

energy muons that might be absorbed before traversing all muon system layers. In either case, a final Kalman filter fit is performed to the hits in both systems.

Muons with transverse momentum below 200 GeV undergo significant multiple scattering in the muon system which reduces the resolution. The tracks are therefore essentially reconstructed using only information from the tracker. At higher momentum, the tracker information is combined with information from the muon system and the full bending power of the magnet can be used for the momentum measurement.

Chapter 4

W and Z boson physics at the LHC

The study presented in this thesis uses measured and simulated samples of Z and J/ψ events to calibrate the muon momentum scale and resolution in the CMS detector. The analysis is part of a high precision measurement of the W boson mass. This chapter introduces the W and Z boson physics of relevance for the presented study and explains how the particles are created and observed at the LHC. The J/ψ meson is presented in Chapter 5.

4.1 W and Z boson production

In a hadron collider such as the LHC, the W and Z bosons are produced at leading order through the annihilation of a quark and an antiquark according to the diagram in Fig. 4.1. The quark and the antiquark each have a fraction of the total proton momentum given by the PDFs and produce a W or Z boson at a partonic center of mass energy equal to the boson mass. The energy scale is thus given by

$$q = \sqrt{s} x_q x_{\bar{q}} = M_{W/Z}, \tag{4.1}$$

where $\sqrt{s}$ is the center of mass energy and x_q and $x_{\bar{q}}$ are the fractional momenta of the interacting quarks.

The cross section for W or Z boson production can be predicted from two components: the PDFs of the proton and the perturbative calculation of the matrix element of the process. Figure 4.2 shows predicted and measured cross sections in CMS for different processes. The rate of a given process is the product of the luminosity and the cross section. Given the LHC nominal luminosity and the measured cross sections, the production rate is around 1 kHz for W bosons and around 300 Hz for Z bosons. The high production rates result in large datasets that allow for detailed measurements.

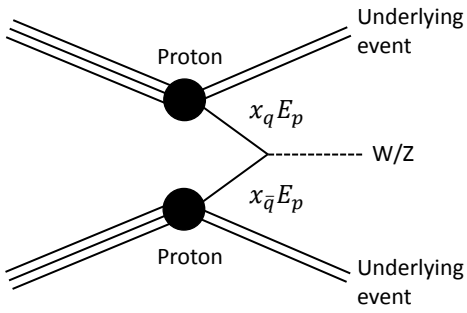

Figure 4.1: A schematic illustration of the W or Z boson production process at the LHC. The interacting quark (antiquark) has an energy $x_q E_p$ ($x_{\bar{q}} E_p$), where E_p represents the total proton energy and x_q ($x_{\bar{q}}$) is given by the PDFs.

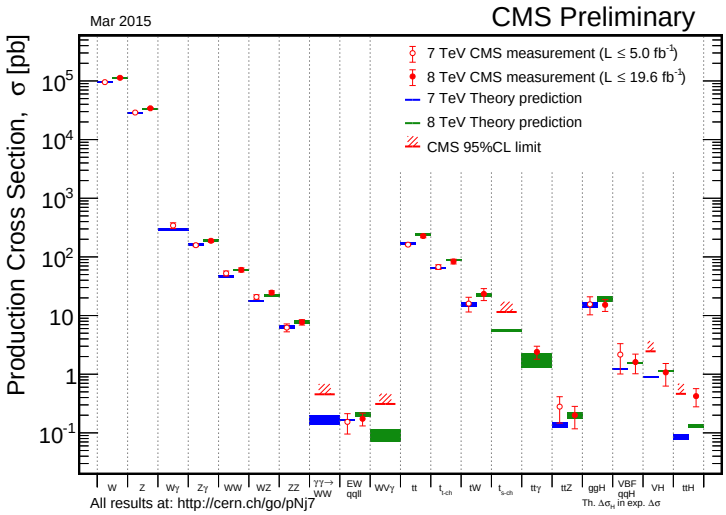

Figure 4.2: Predicted and measured cross sections in CMS for different processes at the LHC at 7 and 8 TeV [21].

4.2 W and Z boson decay

Due to the very limited lifetime, the production of a W or Z boson is instantaneously followed by its decay. The bosons must therefore be detected through their decay products. The probability of a certain decay mode is described by the branching ratio which is defined as the ratio between the rate of the decay mode of interest and the total decay rate of the boson.

The W^+ boson can decay into an antilepton and a neutrino or into an up-type quark and a down-type antiquark, with the exception of the top quark which is too

massive. Similarly, the W^- decays into a lepton and an antineutrino or into an up-type antiquark and a down-type quark. Each leptonic decay mode has a branching ratio of 11 % [6]. The Z boson decays into a fermion and an antifermion of the same flavor. Each leptonic decay has a branching ratio of 3.3 % [6]. Figure 4.3 shows the leading order Feynman diagrams of the production processes of W and Z bosons with the leptonic decay modes.

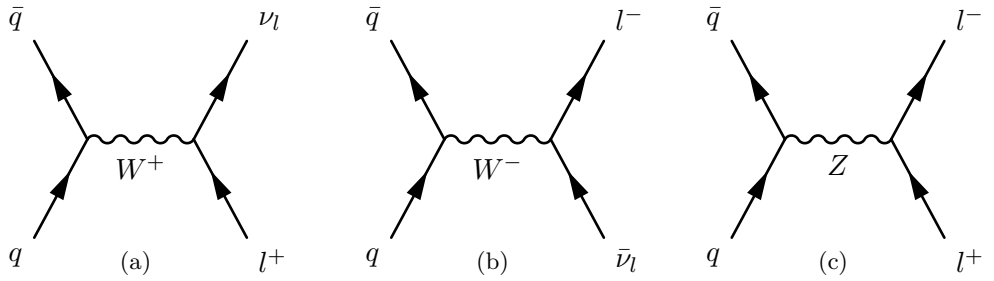

Figure 4.3: Feynman diagrams for the production and leptonic decays of W^+, W^- and Z bosons at the LHC.

The dominant decay mode of the bosons is the hadronic decay. It is however experimentally very difficult to detect the hadronic channels since there is a large background from other processes. The W and Z bosons are therefore observed through their leptonic decays. At CMS, the clearest channel to observe the bosons is the direct muonic decay since the muons can be reconstructed with very high purity as explained in Section 3.2.8.

4.3 W and Z mass distributions

The Z boson mass is fully measurable from the muonic decays since the complete four vectors p_{μ^+} and p_{μ^-} of the two final state particles can be precisely measured. For every event, the dimuon mass is given by

$$M^2_{\mu^+\mu^-} = (p_{\mu^+} + p_{\mu^-})^2 = p_{T_+} p_{T_-} \left[\mathrm{e}^{\Delta\eta} + \mathrm{e}^{-\Delta\eta} - 2\cos\Delta\phi \right]. \tag{4.2}$$

where $\Delta\eta$ and $\Delta\phi$ are the differences in the angles between the two muons. The distribution of this quantity peaks at the invariant mass[1] M_Z and has a width given by the convolution of the Breit-Wigner width, the PDFs and the detector resolution. The mass distribution is also affected by so-called final state radiation (FSR) where the muons radiate off photons. These photons carry away energy from the muons, resulting in a tail on the left side of the peak.

[1]The PDFs fall steeply with energy and give rise to a shift of the peak by about 100 MeV below the nominal Z mass.

For the W boson, the event reconstruction is more complicated. The neutrino can only be inferred from the missing transverse energy and its longitudinal momentum component cannot be measured. This implies that the event has to be reconstructed in the transverse plane. At hadron colliders, the W boson mass is therefore determined from the so-called transverse mass which is defined as

$$M_T = \sqrt{2p_T^l E_T^{\text{miss}} (1 - \cos\phi)}, \tag{4.3}$$

where p_T^l is the transverse momentum of the charged lepton, E_T^{miss} the missing transverse energy and ϕ the angle between the transverse momentum of the lepton and the missing transverse energy. The spectrum of the transverse mass has an edge at the point M_W which is used to measure the mass. Figure 4.4 shows the mass and transverse mass distributions for Z and W respectively, as measured by CMS at $\sqrt{s} = 7\,\text{TeV}$.

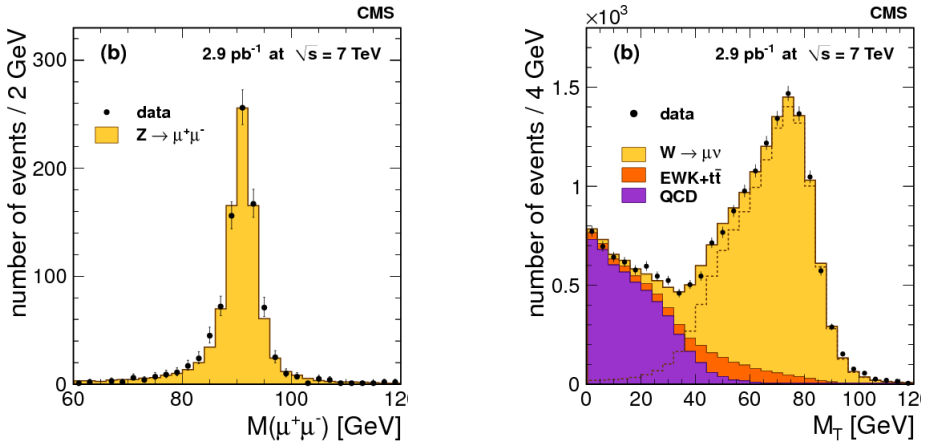

(a) (b)

Figure 4.4: Signal distributions of the muonic W and Z samples collected by CMS at 7 TeV [22]. (a): Dimuon mass spectrum for the $Z \to \mu\mu$ sample. The points represent the data and the histograms represent the simulation. The background is negligible ($< 0.1\,\%$) and is not represented in the plot. (b): Transverse mass distribution for the $W \to \mu\nu$ sample. The points represent the data. Superimposed are the results of fits for the signal (yellow), electroweak background (orange) and QCD background (violet). The dashed lines represent the signal distributions from simulations.

The W muonic sample has a significant background, mainly coming from the decay of b quarks into one muon and a jet of hadrons in the same direction. This background can be separated from the W signal by requiring the muon to be isolated. The Z sample is almost pure signal with a negligible background. Furthermore, the Z boson mass and width are known to high precision. These events are therefore suitable for calibration purposes. The topology of the decay is very similar to the signal $W \to \mu\nu$ and the Z can therefore be used to provide precise information about the production processes of the W.

Chapter 5

The J/ψ meson

The J/ψ particle is the bound state of a charm quark and antiquark ($c\bar{c}$). It has a mass of 3.0969 GeV and a decay width of 92.9±2.8 keV [6]. The J/ψ can be produced in proton-proton collisions via two mechanisms: either as a prompt meson that is directly produced in the primary interaction or as a non-prompt meson produced in the decay of b hadrons. The non-prompt component is characterized by a secondary vertex since the parent particle travels some distance before decaying.

The J/ψ can decay into hadrons, an electron-positron pair or a muon-antimuon pair with a branching ratio of about 6 % for the leptonic decays. The dimuon decays can be reconstructed with high purity and the sample is therefore suitable for calibration purposes. Furthermore, the J/ψ has a negligible decay width compared to the resolution in the CMS detector. The only width seen in the mass distribution stems from the resolution on the measurements of the four-momenta of the decay products. The sample can therefore be used to directly examine the detector effects. Figure 5.1 shows the J/ψ invariant dimuon mass distribution, as measured by CMS at $\sqrt{s} = 7$ TeV.

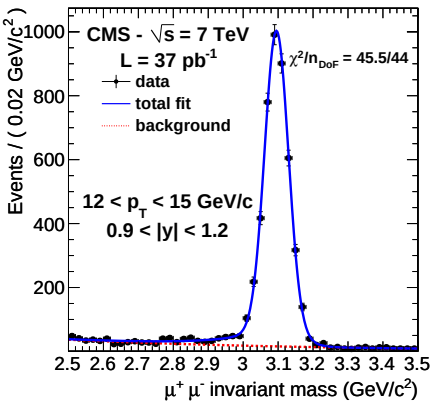

Figure 5.1: The dimuon mass distribution and the result of a fit for the J/ψ peak in the bin: $0.9 < y < 1.2$, $12.0 < p_T < 15.0$ GeV [23].

Chapter 6

W mass measurement

This thesis presents the calibration of the muon momentum measurement in the CMS experiment. The work is part of an analysis aiming for a high precision measurement of the W boson mass where the muon momentum represents one of the main systematic effects. This chapter introduces the general strategy of the W mass measurement and explains the need for a precise calibration of the muon momentum.

6.1 Motivation for the W mass measurement

Any parameter in the electroweak sector of the SM can be predicted from a fit of the model to a few precisely measured observables, as described in Section 2.5.2. Fits of this kind have traditionally been used to constrain free parameters of the SM, such as the Higgs and top masses, before their experimental discovery. Today, all fundamental SM parameters are experimentally determined and the electroweak fit can be used as a powerful tool to assess the validity of the theory and to constrain scenarios for new physics. The level of consistency between the predictions and the experimental values places indirect bounds on non-SM effects that would affect the measurements.

The electroweak fit predicts the W mass to be $80.358 \pm 0.008\,\text{GeV}$ [10] whereas the world average experimental value is $80.385 \pm 0.015\,\text{MeV}$ [6]. Figure 6.1 shows the $\Delta\chi^2$ profile of the electroweak fit as a function of the W boson mass, together with the experimental value. When the errors are taken into account, there is a tension at the level of 1.6 sigma between the prediction and the experimental value. A new measurement of the W boson mass with improved precision would shed more light on the level of consistency between the values and would therefore provide an important test of the SM.

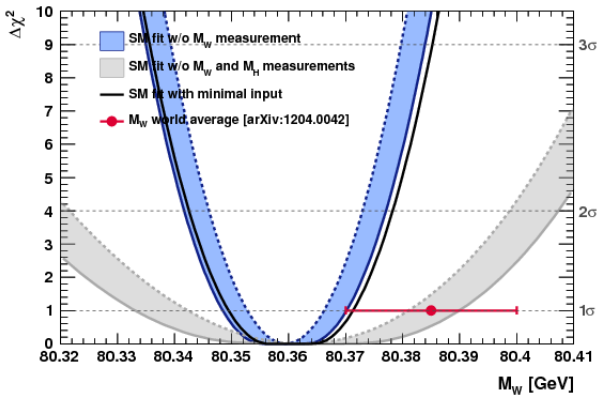

Figure 6.1: $\Delta\chi^2$ profiles for the indirect measurement of the W boson mass [24]. The data point placed along $\Delta\chi^2 = 1$ represents the experimental value and its $\pm 1\sigma$ uncertainty. The grey (blue) bands show the results when excluding (including) the M_H measurement from (in) the fits. The solid black curve represents the SM prediction derived from a minimal set of input measurements.

6.2 General strategy of the W mass measurement

The most precise single W mass measurement to date is quoted by the CDF collaboration at the proton-antiproton collider Tevatron and has an uncertainty of 19 MeV [25]. A detailed description of the CDF measurement can be found in Reference [26]. The first attempt to measure the W boson mass at the CMS experiment follows the same strategy and aims for a similar precision.

At the LHC, the W boson is produced through the annihilation of a quark and an antiquark and is best reconstructed by CMS through its decay into a muon and a muon neutrino, as described in Chapter 4. The W mass is extracted from three experimental quantities based on observables transverse to the beam direction: the muon transverse momentum, the missing transverse energy and the W transverse mass which is a combination of the other two observables with the addition of the angle between them.

The first analysis is carried out on $W \to \mu\nu$ events collected at a center of mass energy of 7 TeV. A template fit is adopted, where the measured distributions of the muon transverse momentum, the missing transverse energy and the transverse mass are compared to Monte Carlo (MC) simulations generated with varying values of the W mass. The value that minimizes the difference between data and simulation is taken as the best estimation of the W mass. In the final measurement, the results of all three fits are combined taking their correlations into account.

6.3 Theoretical and experimental uncertainties

The success of the W mass measurement relies on the assumption that the simulation correctly describes how all relevant quantities depend on the W mass. Two kinds of systematic errors affect the measurement: theoretical uncertainties in the models used to produce the simulated samples and experimental uncertainties on the measurements of the muon momentum and the missing transverse energy. The main theoretical uncertainties are introduced by the PDFs, the FSR corrections to the production process and the simulation of the p_T spectrum of the W boson. Improvement on this part may come from better theory descriptions and better measurements of other quantities used to produce the models.

In order to reduce the experimental uncertainties, it is important to calibrate the transverse momentum and the missing transverse energy in data and MC to remove biases induced by the detector. The two calibrations are performed as separate projects, evolving in parallel. This thesis presents the calibration of the muon momentum with emphasis on the calibration of the muon momentum resolution.

An estimation of the precision needed in the calibration is represented by the precision reached by CDF. The collaboration quotes a systematic error on the W boson mass of 7 MeV due to the lepton momentum scale and a comparably negligible error of 1 MeV due to the momentum resolution [25]. The uncertainty on the muon momentum scale propagates to the W mass measurement with a factor of two. This can be understood by considering the simple example of a W boson decaying at rest into a muon and a muon neutrino. The decay products will be emitted back-to-back with a momentum equal to half of the boson mass. A given error on the muon momentum is therefore multiplied by a factor of two when translated to the W mass. Based on this discussion, the muon momentum scale must be calibrated to an uncertainty of around 4 MeV. The typical momentum of the muon in the W decay is 40 GeV which means that the calibration must reach a relative precision on the order of 10^{-4}.

Chapter 7

Calibration of the muon momentum scale

The level of understanding of the muon momentum scale is one of the main systematic uncertainties affecting the W mass measurement. In order to reach the desired precision on the W mass, the shape of the momentum distribution must be controlled at a level of 10^{-4}. This chapter introduces the general strategy of the calibration of the muon momentum scale, starting with a detailed description of the detector effects that bias the measurement.

7.1 Bias of the muon momentum scale

The transverse momentum of the muon is measured from the sagitta of its track in the magnetic field, as discussed in Section 3.2.4. The track reconstruction is performed using information on the location of each tracker module, on the magnetic field and on the material in the tracker, as described in Section 3.2.6. Flaws in the modeling of these components induce biases in the track reconstruction that then propagate to the momentum measurement. The muon momentum measurement therefore has to be corrected for imperfections in the modeling of the magnetic field and the material in the tracker as well as for misalignment of the tracker modules. The following subsections describe the detector effects that create the biases in the momentum measurement.

7.1.1 Magnetic field

The map of the magnetic field of the CMS solenoid was precisely measured before the experiment was installed in the cavern below ground. However, in order to save computing time, the tracks are reconstructed using a three-dimensional analytic parametrization that approximates the real field map. Figure 7.1 shows the ratio of the field integrals computed with the parametrized and real maps, along a straight line from the origin. The ratio is close to unity but displays variations at a level

of 10^{-3}. Before the calibration of the muon momentum scale, the momentum is corrected for these variations as a function of the coordinates η and ϕ at the origin. This approach implicitly assumes the muon tracks to be straight lines. For the tracker magnetic field of 3.8 T and the radius of around 1 m, the bending angle of a 40 GeV muon is 3 mrad. This is much smaller than the size of the variations in the map in Fig. 7.1 and the approximation of a straight line is therefore appropriate.

The CMS magnet is equipped with six NMR probes that monitor the magnetic field. After the placement below ground, the reading of these probes changed by a factor of 0.9992. It is unclear how this effect propagates through the tracker volume. However, it is plausible that the measured map underestimates the magnetic field by this amount. The transverse momentum is proportional to the magnetic field which means that the underestimation would bias the momentum scale at a level of $8 \cdot 10^{-4}$ which exceeds the desired precision.

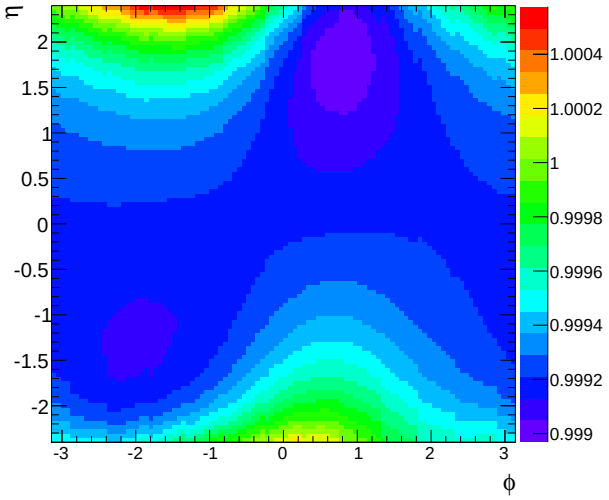

Figure 7.1: Ratio between the parametrized and the measured magnetic field maps in the η-ϕ plane in CMS.

7.1.2 Energy loss in the material

When a muon passes through the tracker it interacts with the electrons in the material, exciting or ionizing the atoms, thereby losing energy. The typical energy loss can be computed from the amount of material in the tracker and the Bethe-Bloch formula which describes the ionization losses of charged particles. For a muon at 40 GeV, the energy loss per unit length and density is $\mathrm{d}E/\mathrm{d}x \sim 2\,\mathrm{MeVcm^2g^{-1}}$. The average density in the tracker is $0.2\,\mathrm{gcm^{-3}}$. The energy lost by a muon along a 100 cm trajectory is therefore around 40 MeV which represents 0.1 % of the initial energy. An imperfect modeling of the material in the tracker exceeding 10 % will therefore affect the momentum measurement at a level above the desired precision.

The density in the tracker is not uniform and the energy loss varies greatly with the pseudorapidity of the muon. Figure 7.2 shows the tracker material budget as described by the simulation of the CMS tracker.

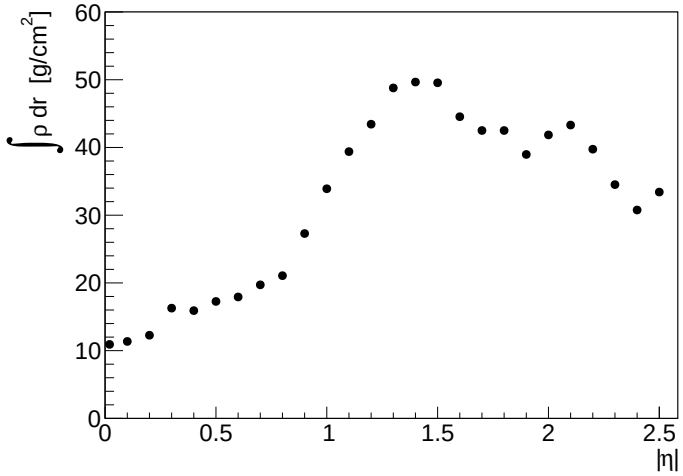

Figure 7.2: Material budget of the tracker. Integrated density along a straight track followed by a particle produced at the center of the tracker as a function of the pseudorapidity.

7.1.3 Misalignment

The alignment of the tracker is described in Section 3.2.7. After the alignment procedure, the statistical accuracy on the module positioning is such that its effect is small compared to the intrinsic measurement precision of the sensors. Smaller differences in the local alignment of individual modules are random and contribute to the resolution on the momentum measurement. The muon momentum scale calibration therefore only has to correct for distortions induced by weak modes, which act in a coherent way.

7.2 Measured and simulated samples

The calibration of the muon momentum scale is performed on measured and simulated samples of J/ψ and Z dimuon events collected at 7 TeV. These events are described in Chapters 4 and 5 and constitute reliable control samples due to their well measured masses and widths. The J/ψ and Z simulated samples used in this analysis are generated, respectively, with PYTHIA6 [27] and with POWHEG [28] interfaced with PYTHIA8 [29].

The J/ψ events are selected at triggering level by requiring two muons with a total transverse momentum of $p_T > 9.9$ GeV and an invariant dimuon mass in the

range $2.8 - 3.35\,\text{GeV}$. In this analysis, both muons are further required to have $p_T > 4\,\text{GeV}$. In 2011, the data taking of prompt J/ψ mesons was limited to the central rapidity region. The data used in this study is complemented with non-prompt J/ψ mesons, which were collected also in the endcaps up to $|\eta| = 2.4$. In the MC, these are not included and the sample is limited to $|\eta| < 1.7$. Figure 7.3 shows kinematic distributions for the J/ψ samples.

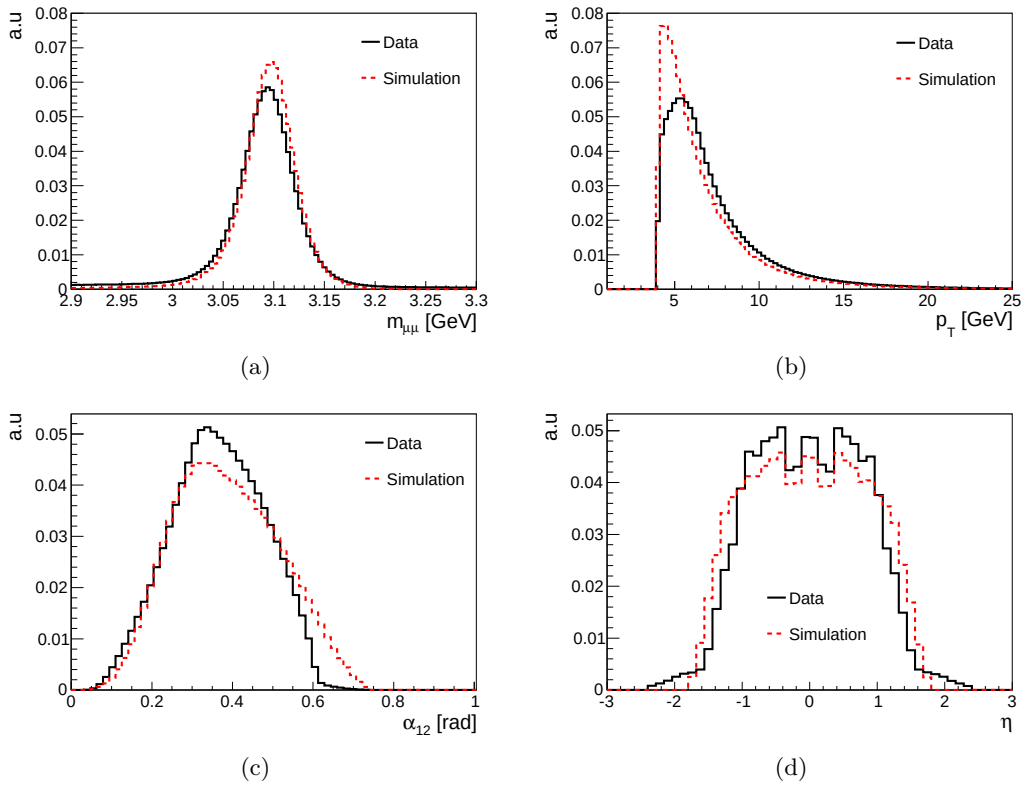

Figure 7.3: Measured (solid black lines) and simulated (dashed red lines) kinematic distributions for dimuon J/ψ decays. (a): Dimuon mass distribution. (b): Transverse momentum of the positive muon. (c): Angle in space between the two muons. (d): Pseudorapidity of the positive muon.

The events in the Z sample are selected at triggering level by requiring a single isolated muon with $p_T > 24\,\text{GeV}$. In the samples used in this analysis, the events are further selected by requiring the most energetic muon to fulfill $p_T > 25\,\text{GeV}$ and the other to fulfill $p_T > 10\,\text{GeV}$. Furthermore, the events are required to have an invariant dimuon mass above $50\,\text{GeV}$. The single muon trigger is limited to $|\eta| < 2.1$. In the data sample used in this analysis an additional cut is applied, limiting both muons to $|\eta| < 2.1$. Figure 7.4 shows the kinematic distributions for the Z samples.

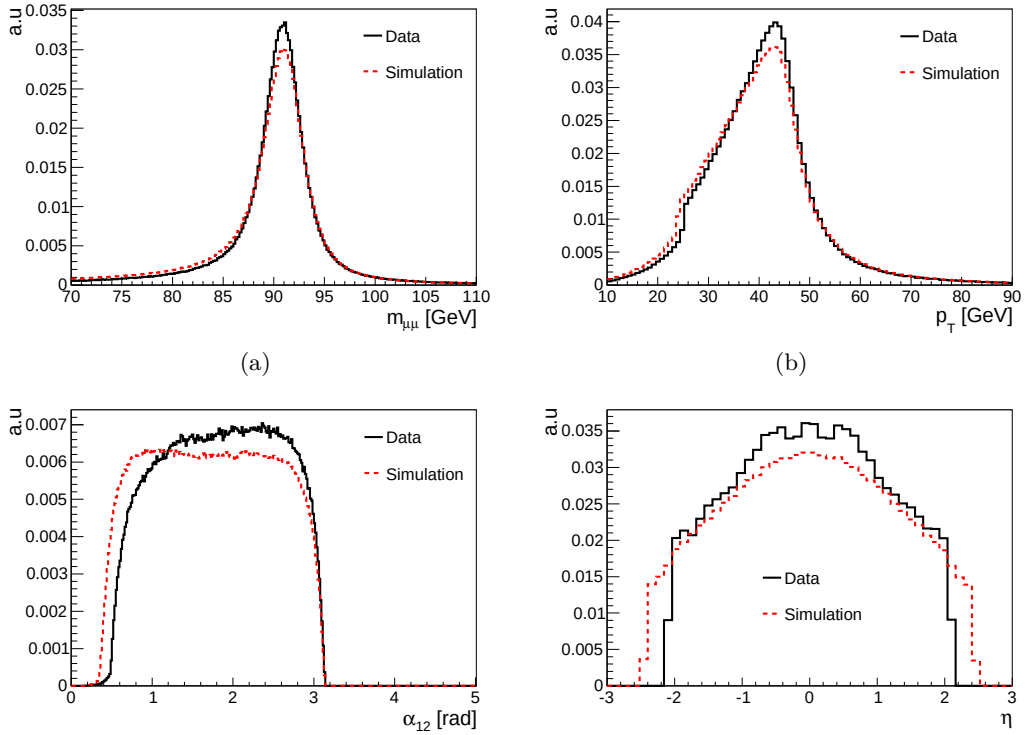

Figure 7.4: Measured (solid black lines) and simulated (dashed red lines) kinematic distributions for dimuon Z decays. (a): Dimuon mass distribution. (b): Transverse momentum of the positive muon. (c): Angle in space between the two muons. (d): Pseudorapidity of the positive muon.

For both the J/ψ and Z samples, clear differences between data and simulation are seen in the distributions. In the J/ψ sample, the differences are mainly due to the trigger threshold at $p_T = 4\,\text{GeV}$ which is not well simulated in the MC. For the Z, they result from the differences in the pseudorapidity cuts applied to the samples. In the calibrations of the muon momentum scale and resolution, data and MC are treated separately. Therefore, the differences do not affect the study.

The distributions in transverse momentum and opening angle between the muons show an important topological difference between the J/ψ and Z samples. For a decay at rest, the muons are emitted with a momentum equal to half of the parent mass. For the J/ψ, these muons cannot be identified since they are absorbed in the large amount of material before the muon system. The selected muons are therefore emitted from highly boosted J/ψ mesons which explains the small opening angle between the two muons.

The mass distributions show differences in the resolution in data and MC. In J/ψ, the mass distribution in the simulation has a smaller width compared to the

data. This implies that the resolution in the simulation is better than the resolution in data. For the Z, the situation is opposite with a better resolution in data compared to the MC. This is an important point for the calibration of the muon momentum resolution, described in Chapter 8.

7.3 Calibration methodology

The calibration of the muon momentum scale is performed using a physics-motivated model that parametrizes the three biasing effects described in Section 7.1 and propagates their effect on the momentum to the dimuon mass. Since the effects are assumed to vary with the geometry of the tracker, the solid angle is divided into bins in η and ϕ. The parameters in each bin are disentangled and extracted from a fit to the mass peak of the control samples. The final result of the calibration is a set of correction factors which can be applied to the muon momentum in each event that enters the W mass measurement.

Parametrization

The calibration of the muon momentum scale is performed using the curvature[1] $k = 1/p_T$ instead of the momentum. The curvature is proportional to the sagitta which is the quantity measured in the tracker and is therefore distributed like a Gaussian function. In each bin in η and ϕ, the measured curvature k is corrected into the curvature k^c accounting for the bias induced by imperfections in the modeling of the magnetic field and the tracker material and by misalignment of the tracker modules.

The parametrization of the three effects is derived on basis of the equation for the momentum of a charged particle in a magnetic field, Eq. 3.8 in Section 3.2.4. In terms of curvature the relation reads

$$k = \frac{1}{qBr}, \tag{7.1}$$

where q is the charge, B the magnetic field strength and r the radius of curvature. According to this equation, a small variation of the magnetic field results in a multiplicative correction factor A to the curvature. The corrected curvature k^c is thus given by

$$k^c = Ak, \tag{7.2}$$

where A is a number close to 1.

An imperfect modeling of the tracker material implies an additional energy loss. The muons considered in the study are ultrarelativistic with $p = E$ and the result is therefore an additive term ϵ to the momentum,

$$p^c = p + \epsilon. \tag{7.3}$$

[1]Normally, the curvature is defined as $1/r$ where r is the radius of curvature. What is called curvature in this analysis is the inverse transverse momentum which is proportional to $1/r$.

This effect can be propagated to the curvature

$$k = \frac{1}{p_T} = \frac{1}{p\sin\theta} \rightarrow k^c = \frac{1}{p^c\sin\theta} = \frac{1}{p\sin\theta + \epsilon\sin\theta} = \frac{k}{1 + k\epsilon\sin\theta}. \tag{7.4}$$

Finally, a misalignment of the tracker modules leads to an additive term to the curvature, opposite in sign for the two muons. This can be understood from the schematic drawing shown in Fig. 7.5. The correction to the curvature can therefore be expressed as

$$k^c = k + qM \tag{7.5}$$

where M is the magnitude of the correction and q is the muon charge.

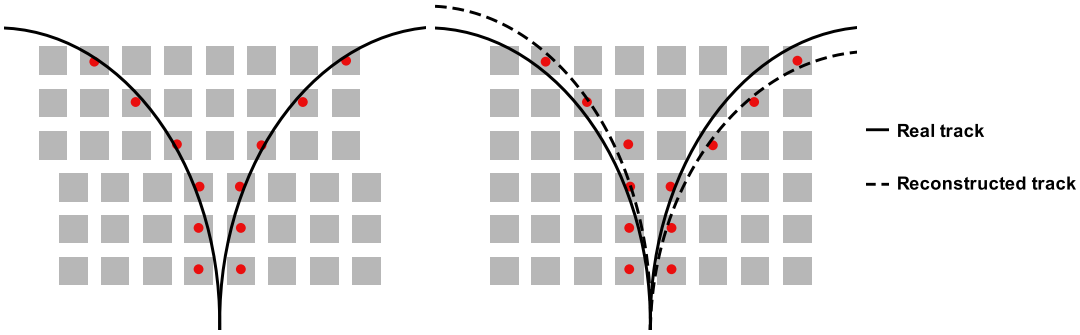

Figure 7.5: Misalignment of the tracker modules. The trajectories of the two muons in the tracker bend in opposite directions due to the magnetic field in the tracker. The actual trajectories in the misaligned tracker (left) will be reconstructed as if the detector was perfectly aligned (right). This leads to an additive term to the curvature, opposite in sign for the two muons.

Accounting for all effects, the combined corrected curvature can be expressed as

$$k^c = (A-1)k + \frac{k}{1 + k\epsilon\sin\theta} + qM, \tag{7.6}$$

where $(A-1)$, M and ϵ are the free parameters determining the corrections in a given bin in η and ϕ. The values of these parameters are expected to be small considering the discussion in Section 7.1. A is expected to differ from 1 by less than 0.001, M is expected to to be less than $10^{-4}\,\mathrm{GeV}^{-1}$ and ϵ is expected to be on the order of a few MeV. These values should be compared to the typical momentum of muons from W decays of around 40 GeV.

The invariant dimuon mass m^2 is given in terms of the curvatures of the two muons as

$$m^2 = \frac{1}{k_+}\frac{1}{k_-}\left[\mathrm{e}^{\Delta\eta} + \mathrm{e}^{-\Delta\eta} - 2\cos\Delta\phi\right], \tag{7.7}$$

where $\Delta\eta$ and $\Delta\phi$ are the differences in the angles of the two muons and $+$ and $-$ denote the positive and the negative muon. The angles are measured with negligible

uncertainty compared to the uncertainty on the curvature [17] and the ratio between the reconstructed mass, which is biased by the detector effects, and the true mass can therefore be expressed as

$$\frac{m^2_{\text{reco}}}{m^2_{\text{true}}} = \frac{k^c_+ k^c_-}{k_+ k_-}. \tag{7.8}$$

With the muons in different bins in η and ϕ, the parameters A, M and ϵ are different for the two muons which results in the relation

$$\frac{m^2_{\text{reco}}}{m^2_{\text{true}}} = \left(A_+ - 1 + \frac{1}{1 + k_+\epsilon_+ \sin\theta_+} + \frac{M_+}{k_+}\right)\left(A_- - 1 + \frac{1}{1 + k_-\epsilon_- \sin\theta_-} - \frac{M_-}{k_-}\right). \tag{7.9}$$

Fit of the correction parameters

The free parameters A, M and ϵ in each η-ϕ bin are extracted from the control samples using a Kalman filter approach[2]. In this case, the system is characterized by a state vector that includes the three parameters in each bin. Every event in the sample is an iteration where the ratio $m^2_{\text{reco}}/m^2_{\text{true}}$ is used to compute the parameters. The target mass m_{true} is taken as the average mass in a sample simulated at generator level. This simulation excludes all detector effects while taking into account important physics effects such as FSR and the mass shift due to the PDFs. The events are weighted using the error given by the covariance matrix of the track reconstruction introduced in Section 3.2.6.

7.4 Closure of the scale calibration

To estimate the closure of the calibration technique, an independent fit model is used to test the result given by the Kalman filter. The closure is described by the ratio

$$r_{\text{abs}} = \frac{m_{\text{true}}}{m_{\text{corr}}}, \tag{7.10}$$

where m_{corr} is the reconstructed dimuon mass after calibration and m_{true} is the invariant dimuon mass in the generator level sample. A perfect calibration takes the reconstructed dimuon mass to the real mass and returns $r_{\text{abs}} = 1$. The deviation from 1 therefore determines the systematic error of the method. The value of r_{abs} is extracted from a fit to the resonance peak using a fit model specifically developed for this purpose. This model is described later, in Section 8.5.1. Since the W mass measurement is performed by comparing data to MC, the important aspect is the relative difference between the samples after calibration. The figure of merit is therefore the ratio

$$r_{\text{rel}} = \frac{r_{\text{abs}}(\text{DATA})}{r_{\text{abs}}(\text{MC})} = \frac{m_{\text{corr}}(\text{MC})}{m_{\text{corr}}(\text{DATA})}. \tag{7.11}$$

[2]The Kalman filter technique is discussed in view of the track reconstruction in Section 3.2.6.

7.5 Resolution effects on the muon momentum spectrum

Apart from the detector effects described in Section 7.1, the muon momentum scale is biased by the resolution on the momentum. This bias can be understood in the following way. Every momentum measurement is made with a corresponding uncertainty. A measurement of a given momentum many times will result in a Gaussian distribution centered at the true momentum and with a width given by the detector resolution. The measured spectrum is the sum of all Gaussians corresponding to the true spectrum. This implies that a given point in the measured spectrum will contain events belonging to the tails of the Gaussians corresponding to the neighboring points in the true spectrum. For a flat distribution, the same amount of events will enter the measured value from both sides and the effect will not create a bias. For a distribution with a slope, like the p_T spectrum, more events enter from one side which leads to a bias in the measured momentum scale.

The bias on the momentum spectrum further propagates to the mass distribution. The Kalman filter technique used to derive the correction factors for the scale is not affected by this bias since the events are compared to the target mass one by one. In the closure test, the full mass distribution is used to extract the scale r_{abs} and any bias introduced by the momentum resolution will therefore affect the result.

The importance of the effect can be examined by performing the closure test on generator level MC which is smeared by adding a resolution to the sample. Since the generator level sample has ideal scale, any bias from 1 in the parameter r_{abs} is a result of the resolution. The smearing of the generator level sample is performed by adding to the curvatures in every event a term randomly sampled from a Gaussian corresponding to the momentum resolution in the MC sample. Figure 7.6 shows the result for different smearings of the generator level Z sample as a function of the transverse momentum of the positive muon in the decay.

The shape of this graph can be understood from the p_T spectrum of the Z, shown in Fig. 7.4(b). The sum of the momenta of the two muons in the decay is constrained by the mass of the Z. For a positive muon with a given transverse momentum below about 45 GeV, the negative muon is at $p_T \gtrsim 45\,\text{GeV}$ where the spectrum has a negative slope. The measured mass is therefore underestimated. For a positive muon with a given transverse momentum above 45 GeV, the negative muon is at $p_T \lesssim 45\,\text{GeV}$ where the spectrum has a positive slope and the measured mass is overestimated.

Clearly, the smearing induces biases in the fitted mass. Of importance for the W mass measurement is the ratio of the closures in data and MC. The mass distributions in Section 7.2 show that the resolution in the simulation differs from the resolution in data for both the J/ψ and Z samples. It is therefore relevant to compare the shift of the mass scale between the different smearings instead of the absolute shift from unity in Fig. 7.6. A difference in the resolution of 10 % causes a non-closure of $2 \cdot 10^{-4}$ which is above the desired level of precision of the scale calibration. Before computing the systematic error of the scale calibration it is

therefore essential to match the resolution in data and MC to avoid this bias. In order to reach a closure of 10^{-4}, the muon momentum resolution in each sample must be measured with a precision at the level of 3 %.

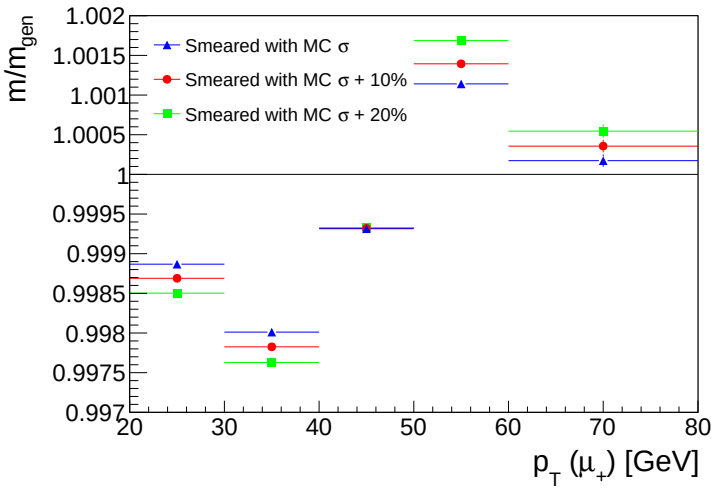

Figure 7.6: Mass shift in smeared Z generator level sample as a function of the transverse momentum of the positive muon. The sample is smeared using different fractions of the resolution σ in the MC, $1 \cdot \sigma$ (blue triangle), $1.1 \cdot \sigma$ (red circle) and $1.2 \cdot \sigma$ (green square).

Chapter 8

Calibration of the muon momentum resolution

The muon momentum resolution plays an important role in the estimation of the systematic error of the muon momentum scale calibration, described in the previous chapter. A difference in the resolution between data and MC gives rise to a bias on the measured mass, resulting in a non-closure of the momentum scale calibration. If the resolution in data and MC is known to good precision, this bias can be removed by correcting the resolution in MC to match the resolution in data. In order to reach the desired precision, the muon momentum resolution must be calibrated to a precision of 3 %. This is a challenging task that requires detailed understanding of the detector and the effects that give rise to the uncertainty on the muon momentum measurement. This chapter describes the calibration procedure starting with a detailed description of the origin of the momentum resolution in the CMS tracker.

8.1 Muon momentum resolution

In the CMS tracker, the momentum[1] of a charged particle is measured from the sagitta of its track, as described in Section 3.2.4. The uncertainty on the momentum measurement therefore depends on the precision that can be achieved on the measurement of the sagitta. For a particle of charge e in a uniform field B, the sagitta s is related to the momentum according to

$$p = \frac{eBL^2}{8s}, \tag{8.1}$$

where L is the length of the track measured on the transverse plane. A given measurement error σ_s can be translated to the momentum using error propagation,

$$\sigma_p = \frac{eBL^2}{8s^2}\sigma_s = p^2\frac{8}{eBL^2}\sigma_s. \tag{8.2}$$

[1] In this chapter, the word "momentum" and the symbol p always refer to the transverse momentum p_T.

The measurement error σ_s stems from two effects: the intrinsic resolution of the measurement points (hits) and the multiple scattering that the charged particle undergoes as it traverses the tracker. These two effects are described separately in the next sections.

8.1.1 Intrinsic hit resolution

All hits in the tracker are measured with an error given by the spatial resolution of the silicon sensors. When the track is reconstructed, these errors are taken into account and are propagated to the track parameters. The resulting uncertainty on the sagitta can be calculated by explicitly minimizing the χ^2 built from the reconstructed track and the hits. This procedure is described in detail in Reference [30]. For the case of N equally spaced measurement points which all have the same resolution ϵ, the uncertainty on the sagitta is given by

$$\sigma_s = \frac{\epsilon}{8}\sqrt{\frac{720}{N+5}}. \tag{8.3}$$

The corresponding error on the measured momentum is obtained by inserting this expression into Eq. 8.2,

$$(\sigma_p)_{\text{hit}} = p^2 \frac{\epsilon}{eBL^2}\sqrt{\frac{720}{N+5}}, \tag{8.4}$$

where the transverse length L in this case is defined by the radial distance between the first and the last measurement point. The relative error is thus proportional to the momentum according to

$$\left(\frac{\sigma_p}{p}\right)_{\text{hit}} = a \cdot p, \tag{8.5}$$

where a is a constant given by

$$a = \frac{\epsilon}{eBL^2}\sqrt{\frac{720}{N+5}}. \tag{8.6}$$

For the CMS tracker, $L \approx 1\,\text{m}$, $N \approx 14$ and $B \approx 3.8\,\text{T}$, as described in Section 3.2.5. The module resolution in the tracker varies between $15 - 50\,\mu\text{m}$ in the various layers. For $\epsilon = 30\,\mu\text{m}$, the above equation predicts a value of $a^2 = 2.6 \cdot 10^{-8}\,\text{GeV}^{-2}$. The value is quoted in quadrature since the momentum uncertainty due to the intrinsic hit resolution later will be added in quadrature to the momentum uncertainty due to the multiple scattering. In the barrel, the value of a is expected to be approximately constant. Tracks in the endcaps above $|\eta| = 1.6$ do not cross the full radius of the tracker and the radial distance between the first and last measurement point decreases. According to Eq. 8.6, the value of a should therefore increase in the endcap. For $|\eta| = 2.5$, the transverse track length is $L \approx 0.4\,\text{m}$ and $a^2 = 1 \cdot 10^{-6}\,\text{GeV}^{-2}$.

8.1.2 Multiple scattering

A charged particle traversing a medium is deflected by many small angle scatters due to Coulomb interactions with the nuclei in the material. The overall deflection angle with respect to the original direction of motion is described by a Gaussian distribution [31]. In the tracker, the width of this distribution gives rise to an uncertainty on the position of the track at each measurement point. This uncertainty can be computed by considering small steps along the path and integrating over the scattering angle at each layer. The corresponding sagitta error can then be inferred from the displacement of the track at each measurement point. These calculations are described in detail in Reference [30]. For a material that is uniformly distributed along the track, the sagitta error is given by

$$\sigma_s = \frac{L}{4\sqrt{3}} \frac{13.6\,\text{MeV}}{p} \sqrt{L/X_0}, \tag{8.7}$$

where L/X_0 is the thickness of the material in radiation lengths. In a non-uniform material, the effect of the multiple scattering on the sagitta is larger if the bulk of the material is at the center of the track. This can be taken into account in the calculation of σ_s by weighting the scattering angle at each step with the square of the distance from the closer endpoint of the segment of length L.

The momentum resolution due to multiple scattering can now be computed from Eqs. 8.2 and 8.7,

$$(\sigma_p)_{\text{ms}} = p^2 \frac{8}{eBL^2} \cdot \frac{L}{4\sqrt{3}} \frac{13.6\,\text{MeV}}{p} \sqrt{L/X_0}. \tag{8.8}$$

The relative resolution is therefore independent of momentum,

$$\left(\frac{\sigma_p}{p}\right)_{\text{ms}} = b, \tag{8.9}$$

where b is a constant defined by

$$b = \frac{2 \cdot 13.6\,\text{MeV}}{\sqrt{3}eBL} \sqrt{L/X_0}. \tag{8.10}$$

Figure 8.1 shows the simulated material of the tracker, expressed in radiation lengths, as a function of the pseudorapidity η and the radius r_s in spherical coordinates. This radius represents the distance in space from the origin, given by $r_s = \sqrt{r^2 + z^2}$ where r and z are the usual cylindrical coordinates. The integral of the material along r_s for a given value of η represents the factor L/X_0 in Eq. 8.10 and can therefore be used to compute the corresponding value of b. Figure 8.2 shows the estimation of b^2 as a function of η, achieved when assuming the material to be uniformly distributed and by accounting for the variations in the material along the track. The plot is by construction symmetric around $\eta = 0$ but is shown for the full range to allow for comparison with results presented later.

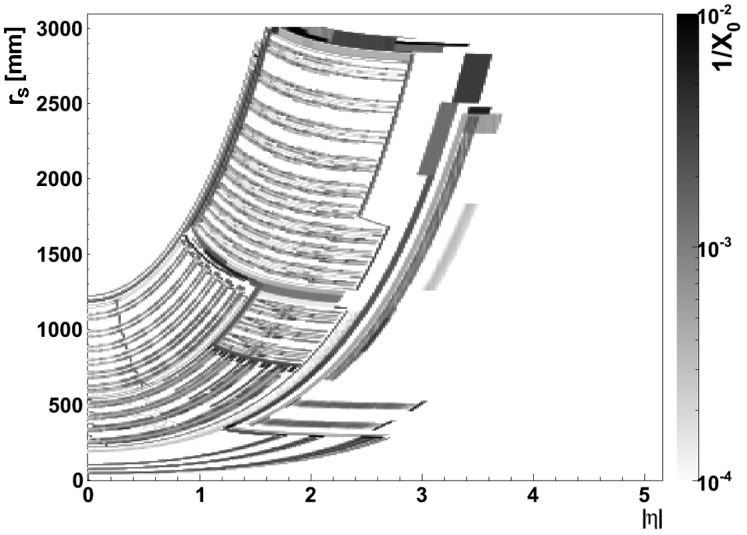

Figure 8.1: Thickness of the tracker material traversed by a particle produced at the center of the detector, in units of radiation lengths, as a function of the pseudorapidity η and the radius r_s in spherical coordinates.

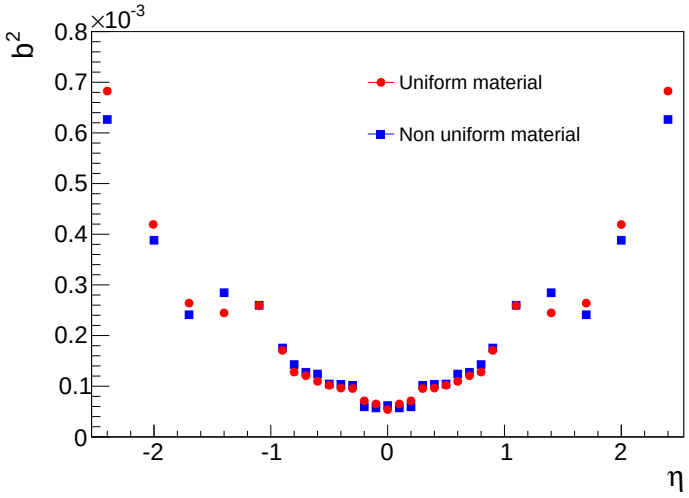

Figure 8.2: Multiple scattering term b^2, as a function of pseudorapidity, computed from the simulated thickness of the tracker material for the assumption of uniform material and by accounting for the non-uniform distribution of the material.

8.2 Parametrization of the muon momentum resolution

The total momentum resolution is the sum in quadrature of the contributions from the hit resolution and the multiple scattering. Based on the discussion in the previous sections, the resolution can therefore be approximated by the functional form

$$\left(\frac{\sigma_p}{p}\right)^2 = \left(\frac{\sigma_p}{p}\right)^2_{\text{hit}} + \left(\frac{\sigma_p}{p}\right)^2_{\text{ms}} = b^2 + a^2 p^2, \tag{8.11}$$

where a and b encode the intrinsic hit resolution and the effect of multiple scattering respectively. This expression suggests that the resolution is dominated at low momentum by the multiple scattering and at high momentum by the intrinsic hit resolution. Figure 8.3 shows a comparison of the two contributions given the value of a^2 for $|\eta| < 1.6$ derived in Section 8.1.1 and the values of b^2 derived in Section 8.1.2 for a non-uniform material.

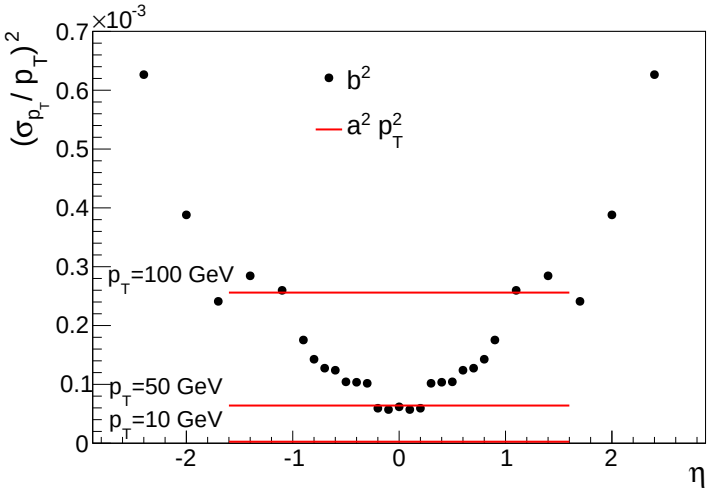

Figure 8.3: Comparison of the two resolution contributions b^2 and a^2p^2 for momenta of 10, 50 and 100 GeV.

In the central region, the resolution is dominated by the multiple scattering up to $p = 50\,\text{GeV}$ where the two effects contribute equally. This implies that muons from the Z decay, which typically have a momentum of 45 GeV, are affected by both contributions to the resolution. For muons from the J/ψ, which typically have a momentum of a few GeV, the resolution is completely dominated by the multiple scattering.

In the previous discussion, the parameter a was estimated by assuming a constant space resolution of the silicon sensors. To examine how crude this approximation is, the a and b parameters can also be extracted from plots of the muon momentum resolution produced with the full simulation of the the CMS tracker.

Figure 8.4 shows the expected relative resolution for single muons of momenta of 1, 10 and 100 GeV as a function of pseudorapidity. The expected resolution is computed by generating many muons at fixed momentum and pseudorapidity and measuring the width of the reconstructed momentum.

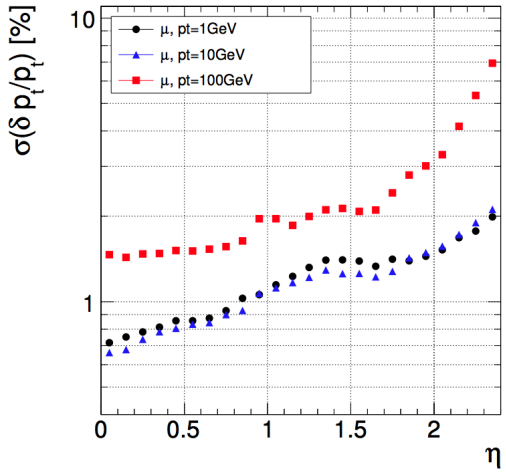

Figure 8.4: Simulated relative resolution on the momentum of the tracker as a function of the pseudorapidity η for muons of momenta of 1, 10 and 100 GeV [15].

At 1 GeV the resolution is entirely dominated by the multiple scattering. The value of b^2 can therefore be obtained directly from the curve at 1 GeV in Fig. 8.4. For $|\eta| = 0$ this approach gives the estimate

$$b^2 \approx \left(\frac{\sigma_p}{p}\right)^2 \approx 4.9 \cdot 10^{-5}.$$

This value is very consistent with the value derived from first principles, shown in Fig. 8.2. The value of a^2 at $\eta = 0$ can be obtained from the curve at 100 GeV by subtracting the value of b^2 from the resolution

$$a^2 \cdot (100\,\text{GeV})^2 \approx \left(\frac{\sigma_p}{p}\right)^2 - b^2 \approx 2.3 \cdot 10^{-4} - 4.9 \cdot 10^{-5} \rightarrow a^2 \approx 1.8 \cdot 10^{-8}\,\text{GeV}^{-2}.$$

This value is 30 % smaller than the value derived in Section 8.1.1. The resolution curve of the 100 GeV muon in Fig. 8.4 also shows that a^2 is approximately constant in the barrel region.

8.3 Muon momentum resolution from the track reconstruction

The final result of the track reconstruction is the set of track parameters and the covariance matrix describing the correlations of the parameters and their errors, as

described in Section 3.2.6. For each dimuon event, the tracking therefore provides estimates of the errors on the muon momenta. These errors are referred to as the event-by-event momentum uncertainties and are computed both for data and MC. The error is estimated by the tracking algorithm using models for the intrinsic resolution of the silicon sensors and the multiple scattering. These models are detailed and simulate the space resolution depending on how the track crosses the sensor.

The accuracy of the model for the resolution, derived in Section 8.2, can be examined by studying the momentum dependency of the event-by-event error. Figure 8.5 shows the squared relative momentum resolution from the track reconstruction as a function of the square of the momentum, in data and simulation, for two different pseudorapidity bins.

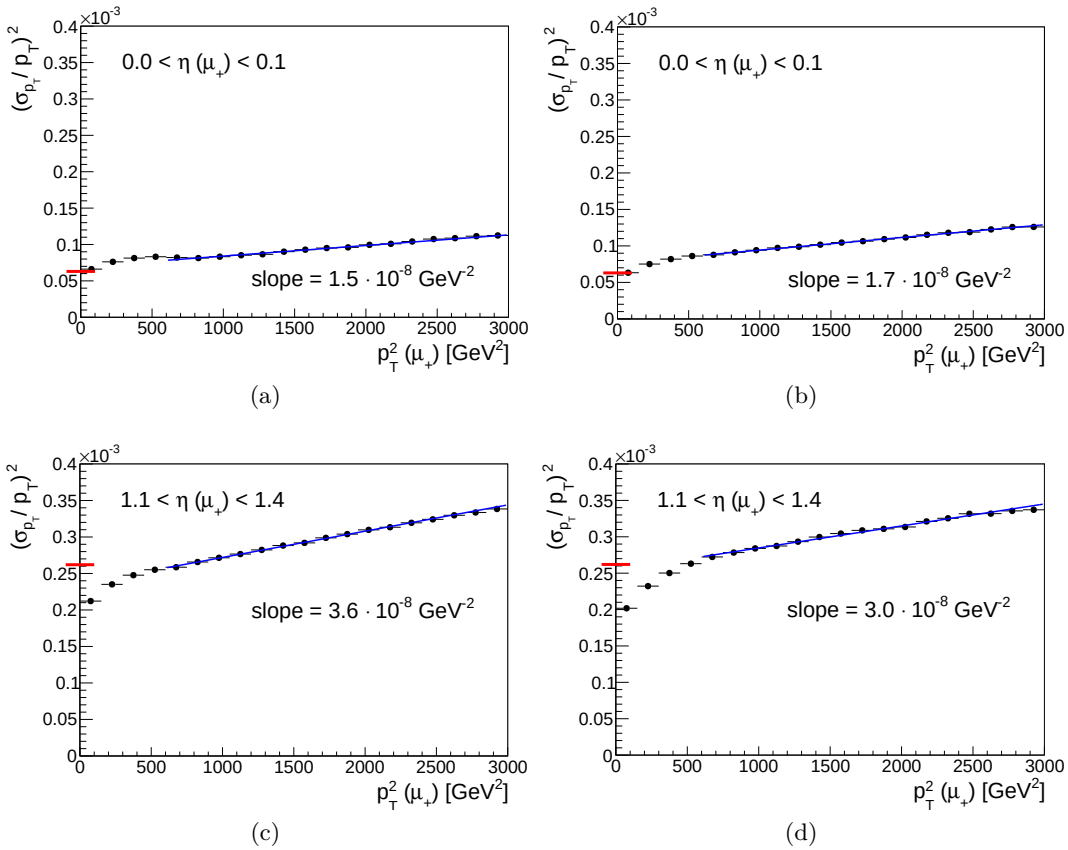

Figure 8.5: Average $(\sigma_p/p)^2$ computed from the event-by-event error of the positive muon in J/ψ and Z dimuon events as a function of p^2 in the bin $0 < \eta < 0.1$ for data (a) and simulation (b) and the bin $1.1 < \eta < 1.4$ for data (c) and simulation (d). The blue curve represents the fit to the points and the red marker the value of b^2 derived for a non-uniform material in Section 8.1.2.

According to the parametrization in Eq. 8.11, these graphs should display a straight line with a slope given by a^2 and an intercept given by b^2. However, the plots show a shift in the slope at around $p^2 = 500\,\mathrm{GeV}^2$. The event-by-event error must therefore have an additional dependence on momentum. It will later be shown that the real resolution also displays this behavior.

A fit with a straight line to the points in Fig. 8.5 above the shift in the slope gives an estimation of the value of the a^2 of the event-by-event error assuming the parametrization in Eq. 8.11. The values for the central bin can be compared to the value derived from first principles in Section 8.1.1. In data, the values differ by about 40 % and in the MC they differ by about 30 %. The graphs in Fig. 8.5 are also complemented with a marker on the y axis showing the expected intercept for the assumed parametrization given the value of b^2 derived in Section 8.1.2.

It is not clear where the additional momentum dependence stems from or how it can be parametrized.[2] A plausible hypothesis is that the effect is related to the angle at which the muon path hits the silicon modules. For large angles of incidence, the charge sharing between two adjacent strips, described in Section 3.2.5, may lead to a larger error on the measurement. This effect is not taken into account in the derivation of the intrinsic hit contribution to the resolution. The angle of incidence is related to the curvature of the track and therefore also to the momentum, which might explain the extra momentum dependency. In this study, the parametrization in Eq. 8.11 will be kept and will eventually be used used to derive corrections to the event-by-event error. This way, the flaw in the parametrization applies only to the correction which is small compared to the resolution.

8.4 Dimuon mass resolution

The muon momentum scale and resolution calibrations are carried out on dimuon events by studying the invariant mass distribution. It is therefore important to understand how the errors on the momentum measurements of the two muons propagate to the dimuon mass

$$m^2 = p_1 p_2 \left[\mathrm{e}^{\Delta\eta} + \mathrm{e}^{-\Delta\eta} - 2\cos\Delta\phi \right], \tag{8.12}$$

where 1 and 2 mark the two muons in the decay. The angles η and ϕ are measured in CMS with a relative resolution on the order of 10^{-3} [17]. Their contribution to the dimuon mass resolution is therefore negligible compared to the momentum resolution. The mass resolution is thus given by

$$\left(\frac{\sigma_{m^2}}{m^2}\right)^2 = \left(\frac{2\sigma_m}{m}\right)^2 = \left(\frac{\sigma_{p_1}}{p_1}\right)^2 + \left(\frac{\sigma_{p_2}}{p_2}\right)^2. \tag{8.13}$$

Using the parametrization in Eq. 8.11, this can be expressed in terms of the a and b parameters. Since the two muons typically are emitted at different η, the

[2] Since the effect is simulated by the MC it can be further examined with a dedicated study, which however goes beyond the scope of this thesis.

parameters are different for the two muons which results in the relation

$$\left(\frac{2\sigma_m}{m}\right)^2 = b_1^2 + a_1^2 p_1^2 + b_2^2 + a_2^2 p_2^2. \tag{8.14}$$

8.5 Measurement of the muon momentum resolution

The calibration of the muon momentum resolution is performed on the measured and simulated samples of J/ψ and Z dimuon events described in Section 7.2. The mass resolution in these samples can be used to extract the momentum resolutions of the two muons in the decay on basis of Eq. 8.13 and also to extract the parameters a and b according to Eq. 8.14.

The momentum resolution varies with the pseudorapidity of the muon. In this study, the η range is divided into 28 bins. It is then assumed that the momentum resolution and the parameters a and b can be taken as constant inside each bin. The task of the calibration is thus to determine the momentum resolution (σ_p/p) in the 28 bins and finally to determine the 28 pairs of parametrization parameters (a, b). Eventually, the derived parameters can be used to equalize the resolution in data and MC on an event-by-event basis in order to avoid biases in the closure test of the scale. The calibration is derived for the region $|\eta| < 2.4$ in data and for $|\eta| < 1.7$ in MC since the J/ψ simulation is limited to this range. For technical reasons, the same binning is used for all samples. The last bin in the Z sample is filled only up to $|\eta| = 2.1$ since the sample is limited to this range.

For a given event, the uncertainty on the mass depends on the pseudorapidities of the two muons in the decay. The samples are therefore split into 28×28 bins in the η_1-η_2 plane. It is important to note that 1 and 2 mark the position in η of a given muon, regardless of its sign. A given bin ij contains all events where the positive muon is in bin i in η_1 and the negative muon in bin j in η_2 as well as all events with the negative muon in bin i in η_1 and the positive muon in bin j in η_2. It therefore holds that a bin ij is equal to a bin ji. For simplicity, the bins are ordered and filled with $\eta_2 > \eta_1$. Figures 8.6 and 8.7 show the population of events in the η_1-η_2 plane with the binning used in the study for the J/ψ and Z samples. The differences between the J/ψ and Z event distributions can be understood from the one-dimensional distributions shown in Section 7.2. In the J/ψ sample, the opening angle between the two muons is small which gives rise to the narrow band of populated bins along the line $\eta_1 = \eta_2$. For the Z, the muons are emitted with a large opening angle and the events populate almost the full η_1-η_2 plane.

The calibration procedure consists of three main steps. First, the mass resolution in each bin ij is extracted from a fit to the mass distribution of the events in the bin. This fit will be referred to as the "mass lineshape fit". The result of the first step is a map of the mass resolution as a function of η_1 and η_2. In the second step, the parameters $(\sigma_p/p)_i$ are extracted from a fit to the map of the mass resolution. This step is referred to as the "momentum resolution fit". Finally, the parameters a_i and b_i are extracted from two separate fits to the mass resolution. The parameters

are derived both accounting for the full resolution and as corrections to the event-by-event error. In the following sections, the various steps of the procedure are described in detail.

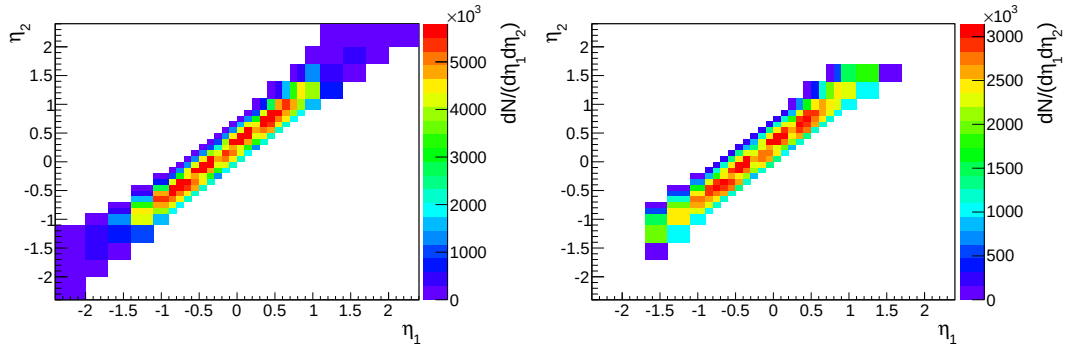

(a) (b)

Figure 8.6: Event distributions showing the correlation between the pseudorapidities of the two muons produced in the decay of J/ψ mesons for data (a) and simulation (b). The distributions are normalized by unit area. The simulation is limited to $|\eta| < 1.7$ and the first and last two bins are therefore empty.

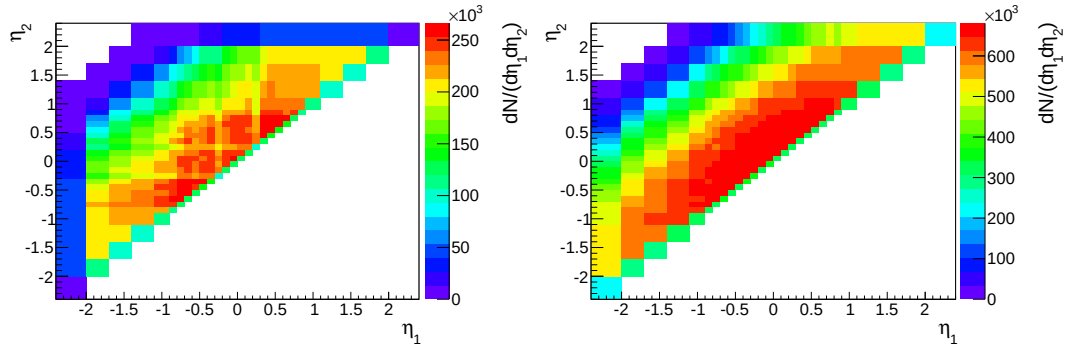

(a) (b)

Figure 8.7: Event distributions showing the correlation between the pseudorapidities of the two muons produced in the decay of the Z boson for data (a) and simulation (b). The distributions are normalized by unit area.

8.5.1 Fit of the mass lineshape

The mass distribution in each bin ij is fitted with a kernel model which is defined by using generator level events that include FSR. Each generator level event contributes to the model with a Gaussian with an average resolution σ and a scale that is a variation of its true scale by a factor r_{scale}. The signal model is thus described by

the probability density function

$$P(m, r_{\text{scale}}, \sigma) = \sum_{i=1}^{N} \frac{1}{\sqrt{2\pi}\sigma} \exp\left[-\frac{1}{2}\left(\frac{m - r_{\text{scale}} \cdot m_i}{\sigma}\right)^2\right], \tag{8.15}$$

where N is the number of events, m_i is the generator level mass of each event and σ is an average resolution appropriate for the sample. The free parameters in the fit are the scale r_{scale} and the resolution σ. This model factorizes out all the theoretical effects such as PDFs and FSR. Since the model builds on generator level events, the width represented by σ is due solely to the resolution of the detector. The model can therefore be used to directly extract the detector resolution from the Z sample where the width of the mass distribution is given by the convolution of the Breit-Wigner width and the detector resolution. Figure 8.8 shows examples of the fits for J/ψ and Z data. The background is modeled by an exponential in the J/ψ sample. In the Z sample, the background is negligible and is not included in the fit.

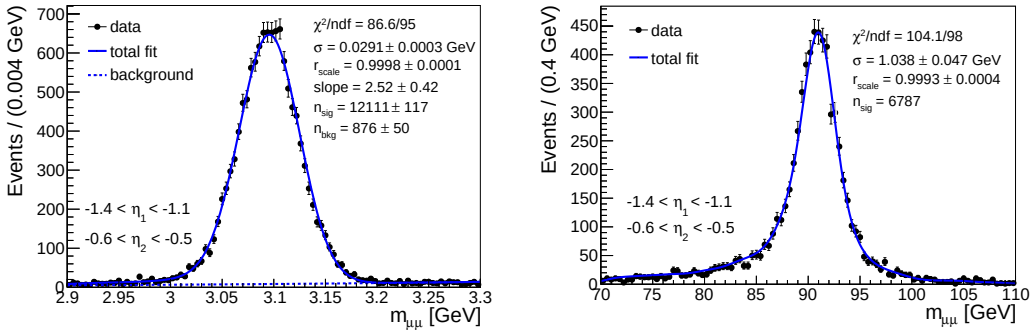

(a) (b)

Figure 8.8: Mass distributions of the J/ψ (a) and the Z (b) data samples in the bin $-1.4 < \eta_1 < -1.1$, $-0.6 < \eta_2 < -0.5$ with the fitted lineshape together with the fit result for the free parameters. The number of events in the signal peak is represented by the parameter n_{sig}. For the fit to the J/ψ, the parameter n_{bkg} represents the number of background events and the slope corresponds to the exponent in the exponential that models the background.

The final result of the mass lineshape fit is a map of the mass resolution in the populated bins. The result is shown in Fig. 8.9 for J/ψ data and simulation and in Fig. 8.10 for the Z. The generator level events used to build the signal model are selected in the same bin ij as the fitted data and have the same momentum cuts applied. All fits are seen to converge with a good χ^2/n_d, where n_d is the number of degrees of freedom. As expected, the resolution is worse in the endcaps, where more material is present and the transverse track length L is shorter. The plots show similar trends in data and MC but the scales differ. For the J/ψ, the resolution in MC is better by $5 - 10\,\%$. For the Z, the resolution in MC is worse by $10 - 20\,\%$. These differences show that the resolution effects indeed would cause a bias in the closure test of the scale calibration.

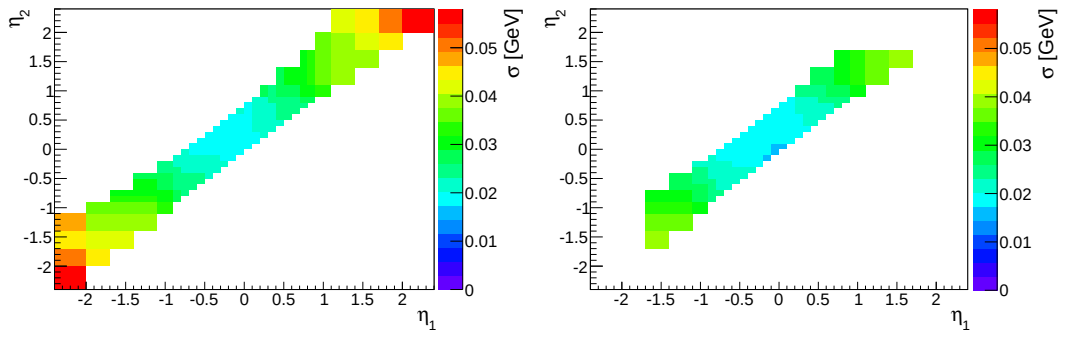

(a) (b)

Figure 8.9: Measured mass resolution as a function of the pseudorapidities of the two muons, for measured (a) and simulated (b) J/ψ events.

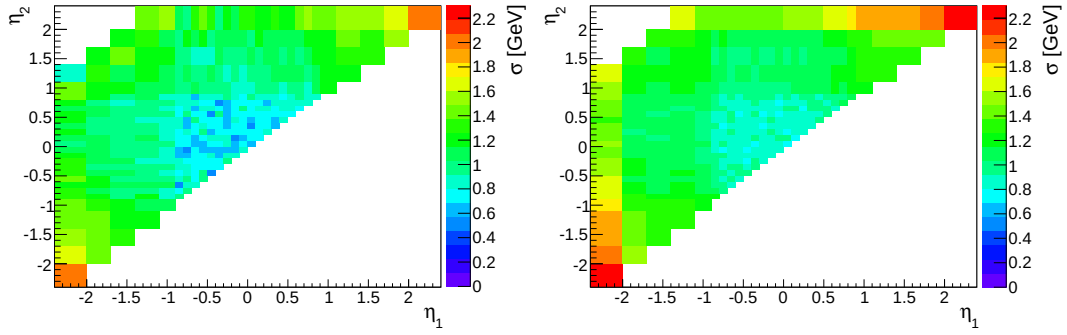

(a) (b)

Figure 8.10: Measured mass resolution as a function of the pseudorapidities of the two muons, for measured (a) and simulated (b) Z events.

Variations of the kernel model can also be used, taking the event-by-event mass uncertainty for each Gaussian kernel and fitting the additional resolution. The signal model is then described by the probability density function

$$P(m, r_{\text{scale}}, \delta\sigma^2) = \sum_{i=1}^{N} \frac{1}{\sqrt{2\pi\left(\sigma_{\text{ebe}_i}^2 + \delta\sigma^2\right)}} \exp\left[-\frac{1}{2}\left(\frac{m - r_{\text{scale}} \cdot m_i}{\sqrt{\sigma_{\text{ebe}_i}^2 + \delta\sigma^2}}\right)^2\right], \quad (8.16)$$

where σ_{ebe} is the event-by-event error and $\delta\sigma^2$ is the correction to be added to the square of the event-by-event error. The free parameters of the fit are in this case the scale r_{scale} and the correction $\delta\sigma^2$ which is allowed to be negative.

8.5.2 Fit of the momentum resolution

In this study, it is assumed that the momentum resolution is constant inside a bin i in η. The mass resolution in each bin ij is therefore a function of the unknown momentum resolutions in the two η bins i and j according to

$$\left(\frac{2\sigma_m}{m}\right)^2_{ij} = \left(\frac{\sigma_p}{p}\right)^2_i + \left(\frac{\sigma_p}{p}\right)^2_j, \tag{8.17}$$

where σ_m denotes the mass resolution obtained from the mass lineshape fit using the first version of the kernel model, Eq. 8.15. The parameters $(\sigma_p/p)^2_i$ can be extracted from a fit to the measurement points $(\sigma_m/m)^2_{ij}$ by adopting the method of least squares. The likelihood function is the χ^2 which in this case is defined by

$$\begin{aligned}\chi^2 &= \sum_{i,j} \frac{\left[\left(\frac{2\sigma_m}{m}\right)^2_{ij} - \left(\frac{\sigma_p}{p}\right)^2_i - \left(\frac{\sigma_p}{p}\right)^2_j\right]^2}{\left[\Delta\left(\frac{2\sigma_m}{m}\right)^2_{ij}\right]^2} \\ &= \sum_{i,j} \frac{\left[\left(\frac{2\sigma_m}{m}\right)^2_{ij} - \left(\frac{\sigma_p}{p}\right)^2_i - \left(\frac{\sigma_p}{p}\right)^2_j\right]^2}{\left(\frac{8\sigma_m\Delta\sigma_m}{m^2}\right)^2_{ij}},\end{aligned} \tag{8.18}$$

where $\Delta\sigma_m$ is the error on the parameter σ_m returned by the mass lineshape fit. The minimum of this equation defines the least-squares estimators for the parameters $(\sigma_p/p)^2_i$. Technically, the minimization conditions

$$\frac{\partial\chi^2}{\partial\left(\frac{\sigma_p}{p}\right)^2_i} = 0 \tag{8.19}$$

reduce the problem to a system of 28 linear equations in the unknown parameters $(\sigma_p/p)^2_i$, which can be solved using matrix algebra. The errors on the fitted points are derived from the covariance matrix U which can be found from its inverse

$$\left(U^{-1}\right)_{ij} = \frac{1}{2}\frac{\partial^2\chi^2}{\partial\left(\frac{\sigma_p}{p}\right)^2_i \partial\left(\frac{\sigma_p}{p}\right)^2_j}. \tag{8.20}$$

The diagonal elements of the covariance matrix represent the square of the errors on the fitted parameters. Figure 8.11 shows the results of the fit for J/ψ and Z after correcting the error bars with a scale factor discussed below.

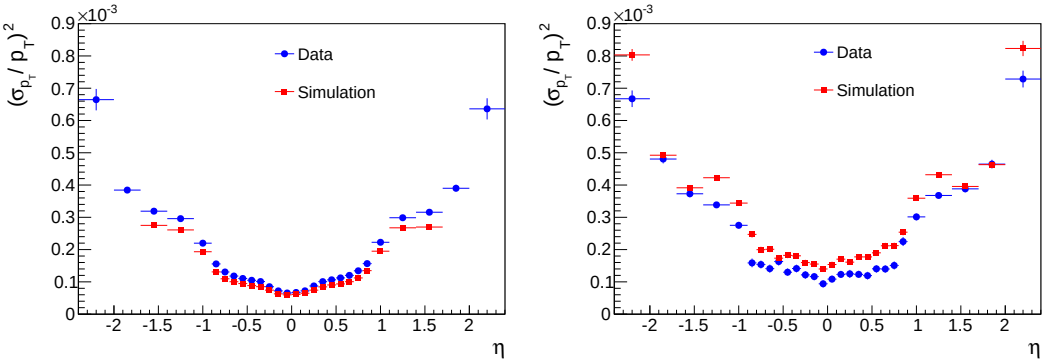

Figure 8.11: Measured relative momentum resolution in J/ψ (a) and Z (b) as a function of pseudorapidity. The error bars on most points are smaller than the marker and therefore not visible.

Goodness of fit

In order to assess the quality of the momentum resolution fit, the total χ^2 is computed according to Eq. 8.18 from the estimated values of $(\sigma_p/p)^2$. A good fit result is characterized by a χ^2 equal to the number of degrees of freedom n_d, which corresponds to the number of measurement points minus the number of fitted parameters. For the momentum resolution fits described in the previous section, the value of χ^2/n_d is 5213/144 for J/ψ data, 2369/132 for J/ψ MC, 530/372 for Z data and 1836/372 for Z MC. These values indicate a poor goodness-of-fit. At the same time, the relative errors on the estimated parameters are found to be very small, on the order of $5 \cdot 10^{-3}$. Given the large value of the χ^2/n_d, these errors cannot be taken at face value.

A poor goodness-of-fit does not necessarily imply large statistical errors for the parameter estimates. The standard deviations of the estimated parameters reflect how widely the estimates would be distributed if the measurement was to be repeated many times, assuming that the hypothesis and the measurement errors used in the construction of the χ^2 are correct. They do not include the systematic error which may result from an incorrect hypothesis or incorrectly estimated measurement errors. It is therefore first important to verify that the errors delivered by the mass lineshape fit are appropriate.

The mass lineshape is essentially a Gaussian for which the statistical error on the width σ is given by $\sigma/\sqrt{N}$ where N is number of events. It is therefore justified to assess the accuracy of the error $\Delta\sigma$ delivered by the mass lineshape fit by comparing it to the ratio $\sigma/\sqrt{N}$. Figure 8.12 shows the ratio of these two numbers in all bins in the J/ψ data sample. The ratio is close to unity which implies that the errors returned by the fit are appropriate. A similar result is seen also in the other three samples.

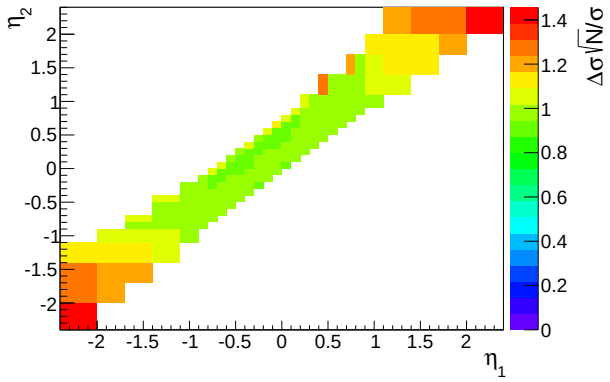

Figure 8.12: The ratio $\frac{\Delta\sigma}{\sigma/\sqrt{N}}$ as a function of η_1 and η_2 for the mass lineshape fit to J/ψ data.

In order to further investigate the large value of the χ^2 of the momentum resolution fit, the contributions from all individual bins are examined separately. These contributions correspond to the terms in the sum in Eq. 8.18. Figure 8.13 shows the χ^2 contributions as a function of η_1 and η_2 for J/ψ data. The distribution shows clear peaks, mostly in the regions around $|\eta| = 1$. In this region, the graph of $(\sigma_p/p)^2$ as a function of η, shown in Fig. 8.11, has a steep slope. Due to this slope, the assumption that the resolution is constant inside the bins in η may fail. Figure 8.14 shows the distribution of the events in the J/ψ data sample in the bin $-1.1 < \eta_1 < -0.9$ when the other muon is selected in different bins in η_2. The distributions are highly non-uniform which explains the poor goodness of the momentum resolution fit. A similar result is seen also in the other three samples.

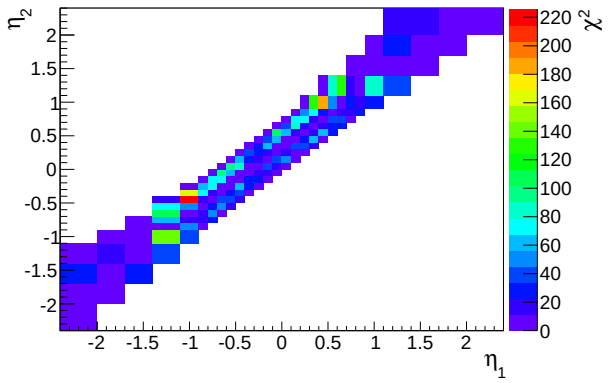

Figure 8.13: Contribution to the total χ^2 as a function of η_1 and η_2 for the momentum resolution fit to J/ψ data.

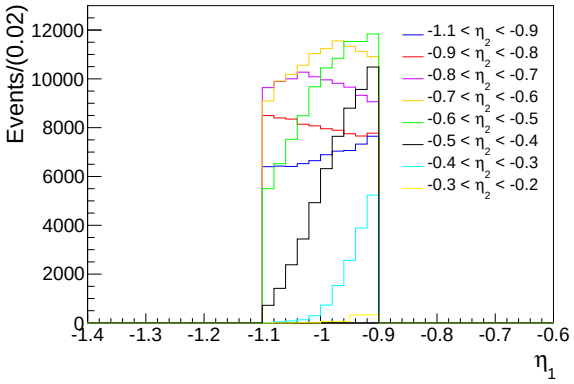

Figure 8.14: Event distributions in η_1 for all populated bins defined by $-1.1 < \eta_1 < -0.9$ for J/ψ data.

In order to obtain error bars that are representative of this bias, the measurement errors entering in Eq. 8.18 are scaled by the corresponding contributions to the χ^2. After the scaling, the values of χ^2/n_d are 150/144 for J/ψ data, 133/132 for J/ψ MC, 342/372 for Z data and 362/372 for Z MC. The estimated parameters are shifted by at most 2 % and the errors are increased by a factor of about 5, resulting in new relative errors on the order of $2-3$ %. The plots presented in the previous section have corrected error bars. In what follows, the errors are always scaled in order to obtain representative error bars.

8.5.3 Fit of the multiple scattering resolution

The method developed in the previous sections can be applied to extract the parameters b_i^2 from the mass resolution. Assuming a constant value of a^2 given by the calculation in Section 8.1.1 and using the average momentum squared in each bin, the χ^2 is built from the equation

$$\left(\frac{2\sigma_m}{m}\right)^2_{ij} = b_i^2 + b_j^2 + a^2_{\text{const}}\left(\langle p_i^2\rangle + \langle p_j^2\rangle\right). \tag{8.21}$$

The fit is performed using only the J/ψ sample in order to reduce the importance of the selected value of a^2. Figure 8.15 shows the results for data and simulation together with the result from the calculation in Section 8.1.2 assuming a non-uniform material.

The importance of the selected value of a^2 can be assessed by varying its value in the fit. A reduced value of a^2 is seen to change the value of b^2 by less than 1 %. Increasing the value by a factor of 2 changes b^2 by 1 % whereas a factor of 5 changes b^2 by 3 %. This can be compared to the relative errors on the values of b^2 which are on the order of $2-3$ %.

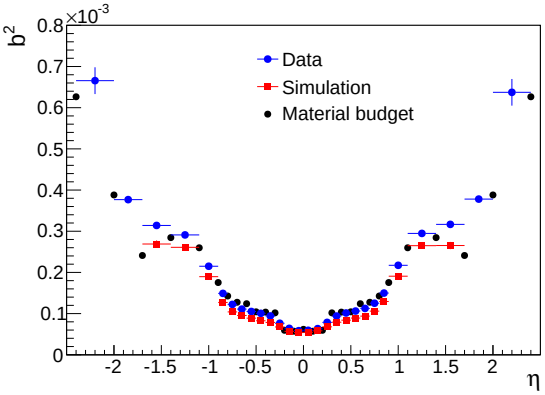

Figure 8.15: Measured multiple scattering term b^2 as a function of pseudorapidity overlayed with the result computed from the material budget of the tracker. The measured results represent the average in each bin whereas the values computed from the material budget represent the results at the given values of η.

8.5.4 Fit of the intrinsic hit resolution

The parameter a^2 can be extracted by considering the difference in mass resolution between two independent samples differing in momentum. The multiple scattering term is independent of momentum and cancels when the mass resolutions in the two samples are subtracted. Using the labels "low" and "high" to mark the sample with the lowest and highest momentum respectively, the mass resolution difference is given by

$$\left[\left(\frac{2\sigma_m}{m}\right)^2_{ij}\right]_{\text{high}} - \left[\left(\frac{2\sigma_m}{m}\right)^2_{ij}\right]_{\text{low}} = \left(a_i^2\langle p_i^2\rangle + a_j^2\langle p_j^2\rangle\right)_{\text{high}} - \left(a_i^2\langle p_i^2\rangle + a_j^2\langle p_j^2\rangle\right)_{\text{low}}. \quad (8.22)$$

The parameters a_i^2 can now be computed by minimizing the χ^2 built from the above equation. The procedure is first performed using only the J/ψ and splitting the sample in two independent samples. All events with two muons of momentum $p > 10\,\text{GeV}$ enter in the high momentum sample and all events with two muons of momentum $p < 10\,\text{GeV}$ enter in the low momentum sample. The procedure is then repeated using the full J/ψ sample as the low momentum sample and the Z for the high momentum sample. This approach allows for the use of the full statistics in both samples and results in smaller statistical errors on the measurement points. The results are shown in Fig. 8.16. It is clear from these figures that the derived values of a^2 differ when computed from the two different samples.

The discrepancy between the derived values of a^2 indicates that the additional dependence on momentum seen in the event-by-event error in Section 8.3 is present also in the measured resolution. The larger value derived from the J/ψ sample corresponds to the steeper slope at low momentum seen in Fig. 8.5 and the lower value derived from both samples corresponds to the less steep slope at high momentum.

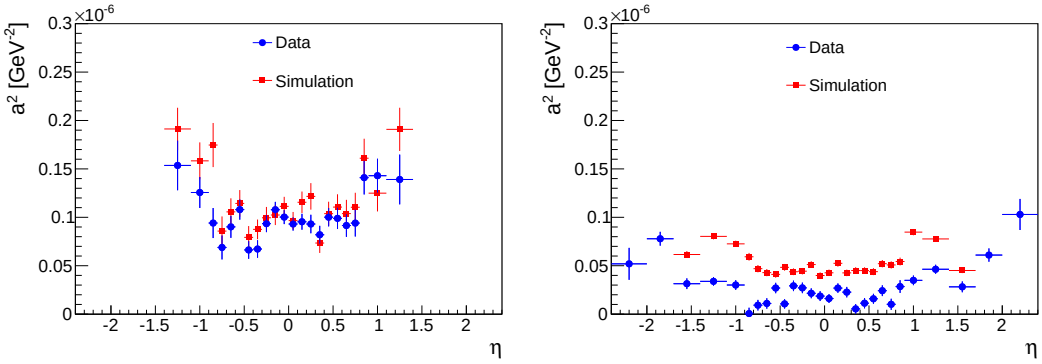

Figure 8.16: Measured intrinsic hit resolution term a^2 as derived from J/ψ (a) and from J/ψ and Z together (b). The result in J/ψ is limited to $|\eta| < 1.4$ due to very large statistical errors in the endcaps.

In order to include the unknown momentum dependence in the resolution calibration, the parameters a^2 and b^2 can instead be extracted as correction factors to the event-by-event resolution.

8.5.5 Correction to the event-by-event error

The correction to the event-by-event error can be derived using the second version of the kernel model, Eq. 8.16, to fit the mass distribution. The result of this fit gives the correction $\delta\sigma^2$ to be added to or subtracted from the event-by-event error in quadrature. This additional resolution can be used to extract correction factors δa^2 and δb^2 that correct the event-by-event error to match the real resolution according to

$$4\left(\frac{\delta\sigma^2}{m^2}\right) = \delta b_1^2 + \delta a_1^2 \cdot p_1^2 + \delta b_2^2 + \delta a_2^2 \cdot p_2^2. \tag{8.23}$$

The parameters δa^2 and δb^2 are computed using the χ^2 fits developed in Sections 8.5.3 and 8.5.4. Figure 8.17 shows the result for the multiple scattering term. This approach represents an alternative way of measuring the flaws in the modeling of the material in the tracker, discussed in view of the scale calibration in Section 7.1.2. Every point in the plot translates into a correction to the amount of material used in the track reconstruction. The correction δb^2 can be compared to the b^2 computed in Section 8.5.3. For the data, the correction is positive in all bins, meaning that the material is underestimated in the track reconstruction. In the barrel, the correction amounts to $2 - 10\,\%$ and in the endcap it amounts to $10 - 20\,\%$. In MC, the correction is negative in the barrel by $1 - 2\,\%$ which implies that the material is overestimated.

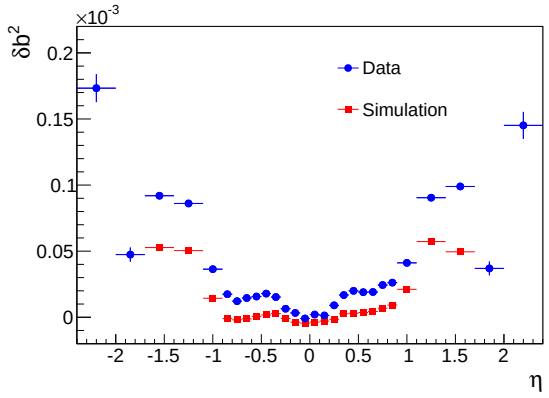

Figure 8.17: Multiple scattering correction δb^2 to the event-by-event error as a function of pseudorapidity.

The result for the intrinsic hit resolution correction is presented in Fig. 8.18 as derived only from J/ψ and from Z and J/ψ together. In this case, the values of δa^2 computed using the different samples are in good agreement in the barrel.

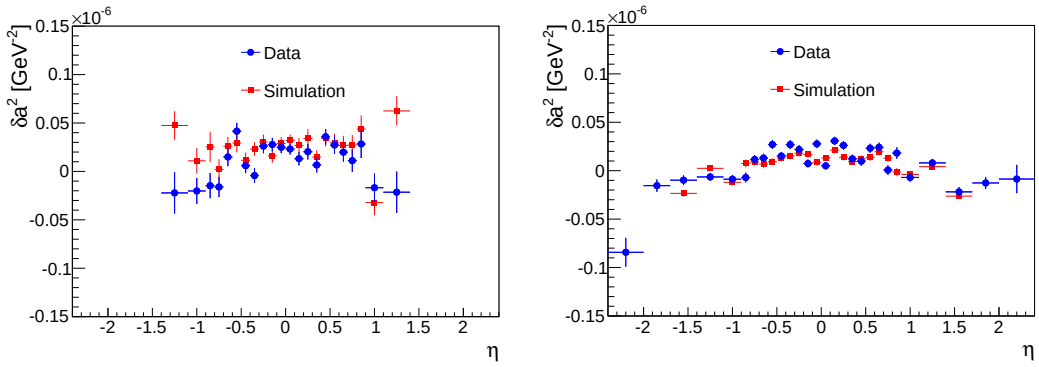

(a) (b)

Figure 8.18: Intrinsic hit resolution correction δa^2 to the event-by-event error as a function of pseudorapidity, as computed from the J/ψ (a) and the J/ψ and Z samples together (b). The result in J/ψ is limited to $|\eta| < 1.4$ due to very large statistical errors in the endcaps.

8.6 Closure of the resolution calibration

The closure of the resolution calibration is derived as a function of the pseudorapidity and the momentum of the positive muon. For each bin, the average resolution is computed from the corrected event-by-event error and compared to the resolution fitted with the simple kernel model, Eq. 8.15. The ratio of these two numbers pro-

vides an estimate of the closure of the calibration method. Figure 8.19 shows the closure before and after the correction to the event-by-event error as a function of the pseudorapidity of the positive muon for the J/ψ samples. After the correction, the event-by-event error matches the fitted resolution to a level of 2 %. Since the resolution in the J/ψ sample is completely dominated by the multiple scattering, this result indicates a systematic error of 2 % on the derived values of δb^2. The closure on the δa^2 term can be computed by comparing the calibrated event-by-event error and the fitted resolution as a function of momentum. Figures 8.20 and 8.21 show the result of the correction in the J/ψ and Z samples as a function of the momentum of the positive muon. After the correction, the event-by-event error matches the fitted resolution to a level of 5 %.

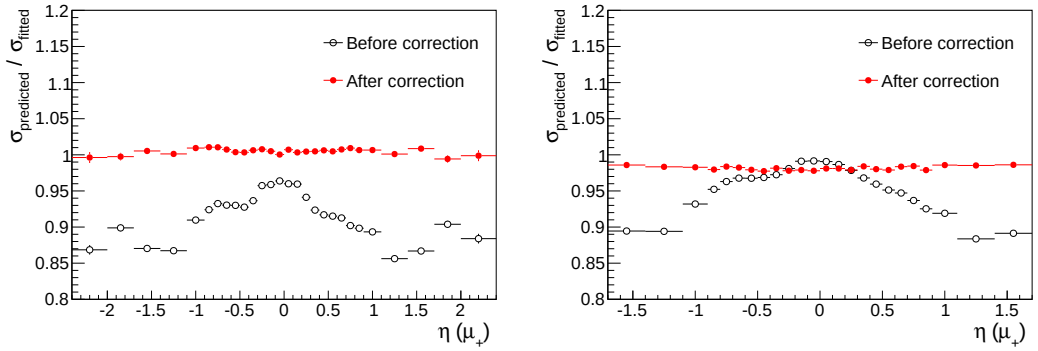

Figure 8.19: Closure as a function of the pseudorapidity of the positive muon before and after correction of the event-by-event error for J/ψ data (a) and simulation (b). The predicted resolution is the average value of the event-by-event error in each bin and the fitted resolution is obtained from the fit to the mass lineshape.

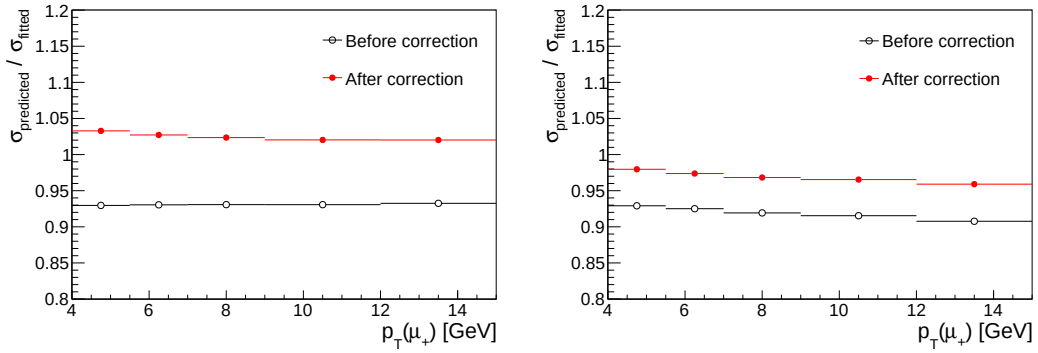

Figure 8.20: Closure as a function of the momentum of the positive muon before and after correction of the event-by-event error for J/ψ data (a) and simulation (b).

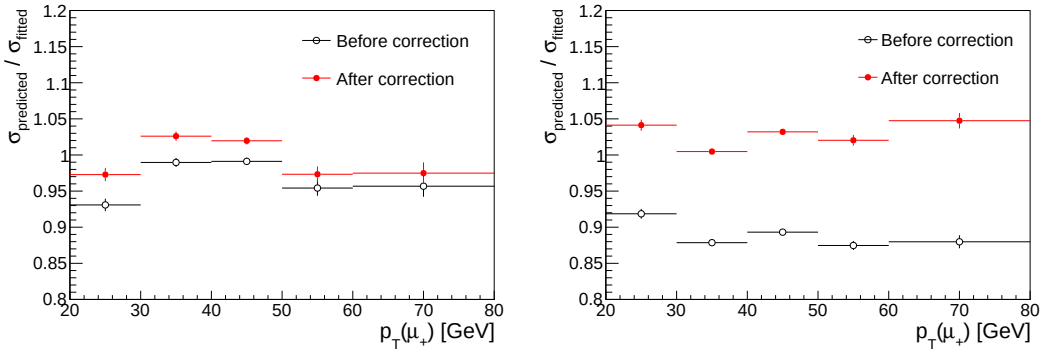

(a) (b)

Figure 8.21: Closure as a function of the momentum of the positive muon before and after correction of the event-by-event error for Z data (a) and simulation (b).

Chapter 9

Summary and conclusions

A precise measurement of the W boson mass allows for an important test of the Standard Model through a comparison between the prediction of the model and the experimental value. In the CMS measurement, the W mass is extracted from $W \to \mu\nu$ events using three experimental quantities based on observables transverse to the beam direction: the transverse momentum of the muon, the missing transverse energy and the transverse mass. A condition for the success of this method is the control of all systematic uncertainties on the distributions of these quantities. This thesis has focused on the calibration of the muon momentum.

The momentum scale is biased by imperfect modeling of the material and the magnetic field in the tracker and by misalignment of tracker modules. In the calibration procedure, these effects are parametrized and extracted from data and simulations of J/ψ and Z dimuon resonances. The measured momentum spectrum is also biased by the resolution which leads to an overestimated systematic error of the scale calibration. In order to remove this bias, the muon momentum resolution must be measured with a precision of 3 %.

This thesis has presented a novel study of the muon momentum resolution as a function of pseudorapidity. The analysis is performed on measured and simulated samples of J/ψ and Z dimuon events collected at a center of mass energy of 7 TeV. The mass resolution in these samples is used to derive correction factors to the event-by-event momentum uncertainty returned by the track reconstruction. After the calibration, the event-by-event error is found to agree with the measured resolution to a level of 5 %, which is slightly above the desired level.

The relative muon momentum resolution is parametrized accounting for two effects: the multiple scattering that the muons undergo when they traverse the tracker and the intrinsic resolution of the tracker modules. The contribution from the multiple scattering is constant whereas the intrinsic hit contribution is proportional to the momentum. In the analysis, an additional momentum dependence is found both in the event-by-event uncertainty and in the real resolution. The effect is neglected in this study but constitutes an important target for further analysis in order to improve the precision of the calibration. Since the additional momentum

dependence is present in the simulation it can be examined with a dedicated study of the MC. Including the effect in the calibration of the momentum resolution may reduce the precision below the desired level of 3 %. Reaching this precision will allow for a reduced systematic error on the muon momentum scale which in turn will increase the precision on the W mass measurement.

Acknowledgements

I would like to express my deepest gratitude to my supervisor at CMS, Luigi Rolandi, for giving me the opportunity to complete my master's degree project at CERN and for guiding me through the work. Most importantly, I would like to thank him for showing me the beauty of physics in every small step of the analysis. I also wish to thank my supervisor at KTH, Jonas Strandberg, for help and support throughout the project. My grateful thanks also go to the W mass group at CMS, and to Michalis Bachtis in particular, for patiently answering my many questions. Finally, I want to show my deepest appreciation to my loved ones for endless support.

List of figures

List of tables

Bibliography

[1] ATLAS Collaboration. Observation of a new particle in the search for the Standard Model Higgs boson with the ATLAS detector at the LHC. *Physics Letters B*, 716(1):1–29, 2012.

[2] CMS Collaboration. Observation of a new boson at a mass of 125 GeV with the CMS experiment at the LHC. *Physics Letters B*, 716(1):30–61, 2012.

[3] S. Weinberg. A Model of Leptons. *Physical Review Letters*, 19:1264–1266, 1967.

[4] S. L. Glashow. Partial-symmetries of weak interactions. *Nuclear Physics*, 22(4):579–588, 1961.

[5] D. Griffiths. *Introduction to Elementary Particles*. Wiley-VCH, Weinheim, 2nd edition, 2008.

[6] K.A. Olive et al. (Particle Data Group). Review of Particle Physics. *Chinese Physics C*, 38:090001, 2014.

[7] G. Breit and E. Wigner. Capture of Slow Neutrons. *Physical Review*, 49:519–531, 1936.

[8] S. Schael et al. Precision electroweak measurements on the Z resonance. *Physics Reports*, 427:257–454, 2006.

[9] P. J. Mohr, B. N. Taylor, and D. B. Newell. CODATA Recommended Values of the Fundamental Physical Constants: 2010. *Reviews of Modern Physics*, 84:1527–1605, 2012.

[10] M. Baak et al. The global electroweak fit at NNLO and prospects for the LHC and ILC. *The European Physical Journal C*, 74:3046, 2014.

[11] L. Evans and P. Bryant. LHC Machine. *Journal of Instrumentation*, 3(8):S08001, 2008.

[12] F. Caola, S. Forte, and J. Rojo. HERA data and DGLAP evolution: Theory and phenomenology. *Nuclear Physics A*, 854(1):32–44, 2011.

[13] Public CMS Luminosity Information. `https://twiki.cern.ch/twiki/bin/view/CMSPublic/LumiPublicResults`. Accessed: 2015-05-14.

[14] Y. Nagashima. *Beyond the standard model of elementary particle physics*. Wiley-VCH, Weinheim, 1st edition, 2014.

[15] The CMS Collaboration. The CMS experiment at the CERN LHC. *Journal of Instrumentation*, 3(8):S08004, 2008.

[16] How CMS detects particles. `http://cms.web.cern.ch/news/how-cmsdetects-particles`. Accessed: 2015-05-14.

[17] CMS Collaboration. Description and performance of track and primary-vertex reconstruction with the CMS tracker. *Journal of Instrumentation*, 9(10):P10009, 2014.

[18] R. Fruhwirth. Application of Kalman filtering to track and vertex fitting. *Nuclear Instruments and Methods in Physics Research*, A262:444–450, 1987.

[19] P. Billoir. Progressive track recognition with a Kalman like fitting procedure. *Computer Physics Communications*, 57:390–394, 1989.

[20] CMS Collaboration. Alignment of the CMS tracker with LHC and cosmic ray data. *Journal of Instrumentation*, 9:P06009, 2014.

[21] Summaries of CMS cross section measurements. `https://twiki.cern.ch/twiki/bin/view/CMSPublic/PhysicsResultsCombined`. Accessed: 2015-05-14.

[22] CMS Collaboration. Measurements of Inclusive W and Z Cross Sections in pp Collisions at $\sqrt{s} = 7$ TeV. *Journal of High Energy Physics*, 1101:80, 2011.

[23] CMS Collaboration. J/ψ and $\psi(2S)$ production in pp collisions at $\sqrt{s} = 7$ TeV. *Journal of High Energy Physics*, 2012(2):11, 2012.

[24] M. Baak et al. The electroweak fit of the standard model after the discovery of a new boson at the LHC. *The European Physical Journal C*, 72(11), 2012.

[25] T. Aaltonen et al. Precise measurement of the W-boson mass with the Collider Detector at Fermilab. *Physical Review D*, 89:072003, 2014.

[26] T. Aaltonen et al. First run II measurement of the W boson mass at the Fermilab Tevatron. *Physical Review D*, 77:112001, 2008.

[27] T. Sjöstrand, S. Mrenna, and P. Skands. PYTHIA 6.4 Physics and Manual. *Journal of High Energy Physics*, 5:026, 2006.

[28] S. Alioli, P. Nason, C. Oleari, and E. Re. A general framework for implementing NLO calculations in shower Monte Carlo programs: the POWHEG BOX. *Journal of High Energy Physics*, 6:043, 2010.

[29] T. Sjöstrand, S. Mrenna, and P. Skands. A brief introduction to PYTHIA 8.1. *Computer Physics Communications*, 178(11):852–867, 2008.

[30] W. Blum, W. Riegler, and L. Rolandi. *Particle detection with drift chambers*. Springer, Berlin, 2nd edition, 2008.

[31] H. A. Bethe. Molière's Theory of Multiple Scattering. *Physical Review*, 89:1256–1266, 1953.